Research Square

Preprints are preliminary reports that have not undergone peer review.
They should not be considered conclusive, used to inform clinical practice,
or referenced by the media as validated information.

SDC2+ foam-like monocytes define a systemic lipid-remodeling program in progressive multiple sclerosis

Howard Weiner

hweiner@bwh.harvard.edu

Brigham and Women's Hospital, Harvard Medical School

Patrick Da Silva

Brigham and Women's Hospital https://orcid.org/0000-0002-3481-4972

Marilia Garcia De Oliveira

Brigham and Women's Hospital

Taha Yahya

Brigham and Women's Hospital, Harvard Medical School

Ronaldo Francisco

Brigham and Women's Hospital

Toby Lanser

Geisel School of Medicine, Dartmouth College

Mahsa Khayat-Khoei

UC Riverside School of Medicine

Christian Barro

Novartis

Maryam Al Mansi

Brigham and Women's Hospital

Jessica Ye

Brigham and Women's Hospital, Harvard Medical School https://orcid.org/0000-0001-8392-7423

Shrishti Saxena

Brigham and Women's Hospital https://orcid.org/0000-0003-3429-5671

Federico Montini

Department of Neurology, Mayo Clinic https://orcid.org/0000-0002-8367-0741

Rohit Patel

BWH https://orcid.org/0000-0001-8432-4616

Jonathan Zurawski

Brigham and Women's Hospital

Somen Mistri

Brigham and Women's Hospital https://orcid.org/0000-0002-2139-6927
Mariann Polgar-Turcsanyi
Brigham and Women's Hospital
Brian Healy
Brigham and Women's Hospital
Laura Cox
Harvard Medical School https://orcid.org/0000-0002-9564-9894
Saef Izzy
MASS GENERAL BRIGHAM https://orcid.org/0000-0002-2822-6736
Rafael Rezende
Brigham and Women's Hospital, Harvard Medical School https://orcid.org/0000-0003-3998-8012
Tanuja Chitnis
BWH https://orcid.org/0000-0002-9897-4422

Article

Keywords:

Posted Date: November 12th, 2026

DOI: https://doi.org/10.21203/rs.3.rs-11354630/v1

License: This work is licensed under a Creative Commons Attribution 4.0 International License.
Read Full License

Additional Declarations: There is **NO** Competing Interest.

TITLE: SDC2+ foam-like monocytes define a systemic lipid-remodeling program in progressive multiple sclerosis

Patrick da Silva[1], Marilia G. Oliveira[1], Taha Yahya[1], Ronaldo Francisco Jr.[1], Toby B. Lanser[2], Mahsa Khayat-Khoei[3], Christian Barro[1], Maryam H. Al Mansi[1], Jessica J. Ye[1], Shrishti Saxena[1], Federico Montini[4], Rohit Patel[1], Jonathan Zurawski[1], Somen Mistri[1], Mariann Polgar-Turcsanyi[1], Brian C. Healy[1], Laura Cox [1], Saef Izzy[1], Rafael M. Rezende[1], Tanuja Chitnis [1], Howard L. Weiner[1].

[1] Ann Romney Center for Neurologic Diseases, Brigham & Women's Hospital, Harvard Medical School, Boston, MA, USA

[2] Program in Quantitative Biomedical Sciences, Geisel School of Medicine, Dartmouth College, Hanover, NH, USA

[3] UC Riverside School of Medicine, Riverside, CA, USA

[4] Department of Neurology, Mayo Clinic, Rochester, MN, USA.

*Corresponding Author:

Howard L. Weiner, MD

E-mail: hweiner@rics.bwh.harvard.edu

ABSTRACT

Progression independent of relapse activity (PIRA) drives irreversible disability in multiple sclerosis, but its immunological basis is incompletely understood. We profiled peripheral myeloid cells from untreated individuals with relapsing-remitting or progressive multiple sclerosis and healthy controls using single-cell RNA sequencing, flow cytometry and untargeted lipidomics. We identified SDC2+ classical monocytes with a foam-like signature that were enriched in progressive disease, increased in patients undergoing PIRA and associated with Expanded Disability Status Scale scores. These cells exhibited increased *LPCAT1* and reduced *PLA2G4A* expression, accompanied by phosphatidylcholine accumulation and lysophosphatidylcholine depletion, consistent with altered Lands-cycle phospholipid remodeling. They also expressed peroxisomal, iron-handling and ferroptosis-associated programs. Human CNS multi-omic datasets revealed analogous *SDC2+LPCAT1+* foam cells enriched in chronic active/inactive white matter and subpial lesions, whereas remyelinating lesions showed partial normalization of this lipidomic signature. These findings define a shared systemic myeloid program associated with chronic, relapse-independent progression in multiple sclerosis.

INTRODUCTION

Multiple sclerosis (MS) is a chronic inflammatory disease of the central nervous system (CNS) in which focal immune-mediated demyelination, neuroaxonal injury and incomplete tissue repair collectively lead to accumulating disability. Although relapses remain an important source of neurological injury in relapsing-remitting MS (RRMS), disability can worsen independently of overt relapse activity, a phenomenon termed progression independent of relapse activity (PIRA). PIRA is increasingly recognized as a major contributor to irreversible disability across the MS disease course and is particularly prominent in progressive MS (ProgMS), yet the cellular and molecular processes that underlie it remain incompletely defined (*1, 2*).

Progressive disease is thought to reflect, at least in part, compartmentalized inflammation within the CNS, including chronic active white matter lesions and cortical subpial lesions. These pathological features contain activated microglia and macrophages, are associated with ongoing demyelination and axonal injury, and correlate with progressive neurological impairment. Chronic lesions are also characterized by oxidative stress, iron accumulation and disturbed lipid handling—processes that can reinforce myeloid-cell activation and tissue injury. However, whether peripheral immune populations reflect or participate in these chronic CNS processes remains uncertain (*3-5*).

Monocytes are well positioned to link systemic immune activity with CNS pathology (*6*). In addition to their established roles in inflammatory signaling, antigen presentation and macrophage differentiation, monocytes can undergo profound metabolic adaptation in response to altered lipid availability and oxidative stress (*7, 8*). Lipid-loaded foam cells are classically associated with atherosclerosis, but related myeloid states have been described in neuroinflammatory and neurodegenerative contexts (*9*). Phospholipid remodeling through the Lands cycle is particularly relevant because lysophospholipid acyltransferases, including LPCAT1, regenerate phosphatidylcholines from lysophosphatidylcholines, thereby influencing membrane composition, lipid storage and inflammatory signaling (*10-12*).

Altered lipid metabolism may be especially consequential in MS because oxidizable phospholipids, iron handling and redox stress can converge on ferroptosis-associated programs (*9, 13, 14*). Ferroptosis is a regulated, iron-dependent process driven by lipid peroxidation, and its molecular machinery intersects with glutathione metabolism, GPX4 activity, membrane phospholipid composition and cellular antioxidant defenses

(*15*). Peroxisomal pathways may further shape these responses by regulating fatty-acid metabolism and reactive oxygen species homeostasis (*16*). These mechanisms have been implicated in inflammatory myeloid-cell states, but their relationship to PIRA, lesion chronicity and progressive MS remains unresolved.

Here, we integrated single-cell transcriptomics, flow cytometry and untargeted lipidomics of circulating monocytes from untreated individuals with RRMS and ProgMS, together with longitudinal analysis of patient who undergo PIRA before and after the observed increase in EDSS score and multi-omic reanalysis of human MS CNS datasets. We identify an SDC2+ classical-monocyte state with foam-like features that is enriched in ProgMS, associated with disability severity and increased during PIRA. We further show that this state is characterized by altered Lands-cycle-associated phospholipid remodeling, peroxisomal and ferroptosis-associated transcriptional programs, and a conserved molecular signature shared with foam cells in chronic white matter and subpial cortical lesions. These findings define a candidate peripheral myeloid correlate of chronic MS progression and nominate lipid remodeling pathways as potential biomarkers and therapeutic targets.

RESULTS

SDC2+ peripheral foam-like classical monocytes are increased in ProgMS and correlate with EDSS and progression independent of relapse activity (PIRA)

We performed single-cell RNA sequencing (scRNA-seq) of ~500,000 myeloid cells enriched from PBMCs samples of 24 untreated MS patients and 6 healthy controls (HC) from the Comprehensive Longitudinal Investigation of MS at Brigham and Women's Hospital (CLIMB study) (**Fig. 1a and Supplementary Table 1**). All subjects were aged and sex matched. Of the MS patients, 10 had RRMS and 14 had non-active ProgMS (no clinical relapse or new T2 or gadolinium lesion on MRI in the previous two years). In total, 5 of the patients sampled experienced a PIRA event (n = 1 RRMS, n = 4 ProgMS). One ProgMS patient had two longitudinal blood samples, one during the incident visit of a PIRA event, and the other 4 years prior. Monitoring the Expanded Disability Status Scale (EDSS) as a summary measure of disability worsening over time, we observe a clear separation of subjects with a relapsing vs. a progressive course (**Fig. 1b**). Because the transcriptomic

monocyte profile of subjects with primary progressive MS (n=5) was identical to those of the secondary progressive (n=9), progressive patients were combined and analyzed together.

We characterized four major cell types: classical monocytes, nonclassical monocytes, intermediate monocytes, and monocyte-derived dendritic cells (mo-DC) (**Fig. 1c**). When we quantified cell number by scRNA-seq, we found an increase in classical monocytes in ProgMS vs. HC (p=0.0033) and a trend in RRMS vs. HC (p=0.056) (**Fig. 1d**). We then measured these cell types by flow cytometry in an independent cohort of 6 HC, 9 RRMS and 14 ProgMS patients and found an increase in classical monocytes in RRMS vs. HC (p=0.036) and a trend in ProgMS vs. HC (p=0.15) (**Fig. 1d**). We also quantified cell number in nonclassical monocytes by scRNA-seq and found that non-classical monocytes from both RRMS (p=0.016) and ProgMS (p=0.0033) were decreased compared to HC (**Fig. 1e**). Using the same independent cohort, we performed flow cytometry and found a decrease in ProgMS vs. HC (p = 0.012) and a trend in RRMS vs HC (p =0.066) (**Fig. 1e**). No differences were observed in intermediate monocytes or mo-DC between MS and HC or between RRMS and ProgMS groups.

Due to the differences observed in the abundance of MS monocytes populations compared to HC, we further characterized them into 4 distinct classical monocytes subpopulations, named after their transcriptional unique profile, as conventional classical, inflammatory, interferon-responsive and foam-like monocytes (**Fig. 1f**). Conventional classical had the same markers as seen in other classical monocyte populations (*CD14*, *S100A8*, *S100A9*, *S100A12*). Inflammatory classical monocytes had high expression of the pro-inflammatory genes *IL1B*, *CXCL8*, *NFKB1* and *NLRP3*. Interferon-responsive classical monocytes over expressed genes associated with interferon priming (*IFI44L*, *IFI44*, *ISG15*, *IFIT1*, *IFIT3*, *MX1* and *OAS3*) compared to the other groups. Foam-like classical monocytes share the transcriptional signature with inflammatory monocytes and in addition have the unique transcriptional markers *EGR2*, *EGR3*, *G0S2*, *CCL3L3*, *IRAK2*, *DUSP2*, *B3GNT5*, *RGCC*, *HBEGF*, *TRIB1*, *PPIF*, *GPR183*, *PTGS2*, *TSPOAP1*, *SDC4* and *SDC2* (**Fig. 1f**). These were termed “foam-like classical monocytes” because of their high expression of syndecan coding genes (*SDC2* and *SDC4*), which are membrane glycoproteins that mediate lipid uptake in macrophages (*17-19*). When we quantified the number of monocytes from scRNA-seq data, the foam-like cells were the only classical monocyte subtype that was increased in ProgMS compared to RRMS and HC (**Fig. 1g,h**). Of note, as shown in **Fig. 1g (highlighted in red)**, we found that there was one subject with RRMS and one subject with ProgMS with a high proportion of foam-

like cells (33 and 47%); both of whom experienced / underwent PIRA. We then performed flow-cytometry of foam-like classical monocytes using SDC2 as a marker, to validate our scRNA-seq analysis and found an increase in SDC2+ monocytes in ProgMS vs. RRMS and vs. HC (**Fig. 1i**). Furthermore, the percentage of SDC2+ cells in total monocytes positively correlated with EDSS score (**Fig. 1i**). Consistent with these findings, the SDC2 mean fluorescence intensity (MFI) on classical monocytes was increased ProgMS vs. RRMS and was positively correlated with EDSS (**Fig. 1j**). The gene expression levels of the foam-like cell markers *SDC2*, *G0S2*, *EGR2*, *CCL3L3*, *B3GNT5*, *TSPOAP1*, *HBEGF*, *PTGS2*, *TRIB1* and *PPIF* were upregulated in ProgMS (n=14) vs. RRMS (n=10) and HC (n=6) (**Fig. 1k**). We then analyzed samples from subjects undergoing PIRA (n=5; 1RRMS and 4 ProgMS) and found that all foam-like cell markers (except *CCL3L3),* were upregulated in PIRA vs. RRMS and vs. HC (**Fig. 1l**). In the ProgMS patient sampled four years prior to and during the onset of PIRA, there was a marked increase in the percentage of foam-like cells, from 0.20% to 9.36% (**Fig. 1m**), in peripheral blood. This shift occurred in association with an increase in EDSS score from 6.0 to 6.5. Differential gene expression analysis of classical monocytes from these two timepoints, focusing on foam-like cell markers, identified *SDC2* as the most strongly upregulated gene associated with PIRA (**Fig. 1n,o**). In summary, SDC2+ foam-like classical monocytes are increased in ProgMS patients and correlate with EDSS and PIRA.

ProgMS classical monocytes accumulate phosphatidylcholine through Lands cycle.

To characterize the foam-like cell subpopulation, we performed differential expression analyses for the following groups: (i) foam-like cell markers; (ii) ProgMS vs. RRMS patients; and (iii) the longitudinally-samples subject pre vs. post PIRA. We performed pathway enrichment analysis on the upregulated differentially expressed genes for each comparison and identified pathways commonly enriched across all three analyses. The majority of commonly enriched pathways were associated with lipid metabolism and fat cell differentiation (**Fig. 2a**), which is consistent with our identification of the increased classical monocyte subtype as foam-like cells. We then employed untargeted lipidomics to investigate the whole lipid profile of classical monocytes from an independent cohort of patients with ProgMS (n=10) and RRMS (n=6). As shown in **Fig. 2b,** the lipidome profile of ProgMS classical monocytes was completely separated from RRMS by PCA analysis. Differential metabolite analysis showed downregulation of lysophosphatidylcholines (LPC) and increased phosphatidylcholines (PC) in ProgMS classical monocytes vs. RRMS (**Fig. 2c,d**). The CDP-Choline pathway

(Kennedy pathway) and the Lands cycle are the main metabolic pathways involved in PCs synthesis (*20-23*). In the CDP-choline pathway, choline is phosphorylated and activated to CDP-choline, which donates its phosphocholine head group to diacylglycerol to form phosphatidylcholine (*22*). By assessing the differential expression of CDP-Choline pathway-associated genes in classical monocytes, most of the genes were downregulated in both samples from subjects with ProgMS and patients undergoing PIRA compared to RRMS and HC (**Extended Data Fig. 1a**). The differential gene expression analysis at the cell type level showed downregulation of these same genes in foam-like monocytes compared to all other classical monocytes subtypes (**Extended Data Fig. 1b**). In the Lands cycle, lysophospholipid acyltransferases reacylate lysophospholipids with long-chain fatty acids to regenerate phospholipids, whereas phospholipases hydrolyze phospholipids to release long-chain fatty acids and generate lysophospholipid intermediates (**Extended Data Fig. 1c**). The differential gene expression analysis of Lands cycle genes comparing foam-like cells with the other classical monocyte subpopulations revealed upregulation of *LPCAT1*, which encodes a lysophosphatidylcholine acyltransferase, and downregulation of *PLA2G4A*, which encodes one of the major phospholipases A2 in myeloid cells. Similarly, classical monocytes from subjects with ProgMS and patients undergoing PIRA presented upregulated *LPCAT1* and downregulated *PLA2G4A* compared to classical monocytes from both subjects with RRMS and HC (**Fig. 2e**). When we compared gene expression of classical monocytes from the longitudinally-sampled ProgMS subject pre and post PIRA, we found that *LPCAT1* expression was increased and *PLA2G4A* decreased during PIRA vs. four years earlier (**Fig. 2f**). These transcriptomics analyses together with the lipidomic profile of ProgMS classical monocytes demonstrate that LPCs and arachidonate (FA(20:4)) are being converted to PCs by altering the Lands cycle, and not the CDP-choline pathway. Analysis of serum untargeted metabolomics from HC, stable RRMS (StRRMS), RRMS that transitioned to ProgMS (TRRMS) and ProgMS samples, recently published by our group (*24*), showed decreased LPC and arachidonate in ProgMS serum compared to the other groups (**Fig. 2g,h**). In summary, these findings may indicate that classical monocytes could incorporate LPCs and arachidonate from serum, to later convert them into PCs by altering the Lands cycle in ProgMS and patients undergoing PIRA.

Foam-like cells and classical monocytes associated with ProgMS and PIRA exhibit peroxisomal activity and ferroptosis transcriptional program activation

To determine how the lipid metabolism modifications we observed in ProgMS classical monocytes drive the foam-like cells expansion, we investigated other enriched pathways using the approach we employed in **Fig. 2a**. We identified pathways associated with inflammation including interleukin-1, TNFα, NFκB and prostaglandin signaling pathways (**Fig. 3a**). The activation of these pathways is consistent with the transcriptomic profile of foam-like cells, which overexpress pro-inflammatory genes, similar to the inflammatory monocyte signature we described in **Fig. 1f**. In addition, we observed enrichment of several pathways related to peroxisomal activity, including intracellular pH regulation and the response to oxidative stress induced by reactive oxygen species such as hydrogen peroxide (**Fig. 3a**). We then analyzed gene expression of peroxisomal activity associated genes and found them highly upregulated on foam-like cells compared to all the other classical monocyte subtypes (**Fig. 3b**). This upregulation was also seen when we compared classical monocytes of patients undergoing PIRA and of ProgMS patients to those of RRMS patients (**Fig. 3c**). Another group of pathways we found enriched was associated with iron uptake and ferroptosis (**Fig. 3a**). Several genes associated with ferroptosis, including *SLC11A1*, *STEAP4*, *SLC25A37*, *PCBP2*, *FTH1* and *FTL* were upregulated in PIRA and ProgMS vs. RRMS (**Fig. 3d**). *TFRC* and *FLVCR2* genes, which encode iron uptake transporters, were highly upregulated in PIRA classical monocytes (**Fig. 3d**). When we compared the ferroptosis associated gene expression amongst the different subtypes of classical monocytes, foam-like cells exhibited upregulation of *GPX4*, *SLC11A1*, *STEAP4*, *SLC25A37*, *SLC39A8*, *PCBP2*, *FTH1* and *FLVCR2* compared to other classical monocyte subtypes (**Fig. 3e**). These findings demonstrate that classical monocytes from MS patients with PIRA and the differentiated foam-like cells enriched in ProgMS have activation of ferroptosis and peroxisome activity transcriptional programs. This indicates increased iron uptake associated with intracellular redox imbalance.

Chronic MS white matter lesions have increased foam cells and accumulation of lecithins

We then asked whether myeloid cells in the CNS of MS patients exhibited findings similar to what we observed in peripheral blood monocytes. We analyzed a snRNA-seq dataset from postmortem human brain samples (NCBI BioProject PRJNA544731) (*25*), that included control white matter (CWM), acute lesions (AL) and chronic active/inactive lesions (CA/CI). Chronic lesions are associated with non-relapsing disease progression in MS, whereas acute inflammatory lesions are characteristic of RRMS (*26, 27*). We analyzed

myeloid nuclei from the dataset and identified four cell types: homeostatic microglia, MGnD microglia (microglial neurodegenerative phenotype), monocytes and foam cells (**Fig. 4a**) using the markers shown in **Fig. 4b**. The brain foam cells had the identical transcriptional signature we found in peripheral foam-like cells, including high expression of *SDC2* (**Fig. 1f and 4b**). Analysis of the myeloid cells showed enrichment of foam cells in the CA/CI lesions compared to AL and CWM (**Fig. 4a**). Next, we examined the myeloid cell transcriptional profile for Lands cycle genes and found upregulation of *LPCAT1* in CA/CI compared to CWM and AL (**Fig. 4c**). We found t upregulation of *LPCAT1* in foam cells compared to monocytes, homeostatic and MGnD microglia (**Fig. 4c**). *MBOAT7*, which encodes another acyltransferase acting on the Lands cycle, showed a similar transcriptional profile to *LPCAT1* in both comparisons (**Fig. 4c**). The phospholipase encoding gene *PLA2G4A* had reduced expression in CA/CI vs. CWM, but no changes in foam cells compared to other myeloid cell types (**Fig. 4c**). This CNS transcriptional signature is similar to the Lands cycle signature we observed in blood foam-like cells associated with ProgMS and PIRA (**Fig. 2e,f**). We then assessed genes associated with ferroptosis and found them upregulated in CA/CI myeloid cells vs. CWM and AL myeloid cells (**Fig. 4d**). Foam cells exhibited upregulation of the ferroptosis associated genes *GSS, SLC11A1, SLC7A11, TFRC, SLC39A8* and *PCBP2* compared to all other myeloid cell types (**Fig. 4d**). We then performed transcriptional analysis of peroxisome activity in brain myeloid cells and found upregulation of 16 genes in CA/CI vs. CWM and AL (**Fig. 4e**). CNS foam cells had increased expression of 15 genes associated with peroxisome activity compared to all other brain myeloid cell types (**Fig. 4e**). When we performed independent analysis of a second postmortem human white matter snRNA-seq dataset (*28*), comparing CWM, normal appearing white matter (NAWM) and MS demyelinated white matter (DMWM), and found similar results (**Extended Data Fig. 2**). In summary, MS chronic lesions have increased foam cells compared to control brain tissue and acute lesions, and these foam cells have a similar transcriptional signature as the blood foam-like cells we describe above including Lands cycle, ferroptosis and peroxisome activity.

We then performed spatial transcriptomic analysis (spRNA-seq) of the foam cells markers we identified to determine their localization with CND pathology. To accomplish this, we analyzed a spatial transcriptomics dataset and compared CWM, NAWM, CA and CI (GEO accession code GSE208747) (*29*). We first assessed the transcriptional location of spots expressing both *SDC2* and *LPCAT1* overlayed with microscopy images stained with Luxol Fast Blue (LFB). We found that CWM and NAWM had few spots that co-expressed *SDC2* and

LPCAT1, whereas CA and CI had a larger number of *SDC2+LPCAT1+* spots (**Fig. 4f**). In CA tissue, the *SDC2+LPCAT1+* spots were localized in demyelinating lesions, while in CI tissue, they tended to surround the demyelinating lesions (**Fig. 4f**). Differential expression analysis showed increases in both *SDC2* and *LPCAT1* expression in CA and CI vs. CWM and NAWM (**Fig. 4f**). To validate these findings, we performed the same analysis on an independent postmortem human white matter snRNA-seq/spRNA-seq dataset, that included CWM, CA and CI samples (*30*), and obtained similar results, with increased *SDC2+LPCAT1+* spots in CA and CI vs. CWM, especially around demyelinated tissue (**Extended Data Fig. 3**). These results indicate that the foam cells we identified in the blood that express SDC2 and LPCAT1 are associated with chronic MS lesions.

We then asked whether the lipidomic signature we identified in the blood of ProgMS was also observed in the CNS. To do this, we analyzed a postmortem brain metabolomics dataset, comprising samples from CWM, NAWM, chronic lesion core, CA and CI edges (*31*). We found reduced arachidonate, choline, phosphocholine and lysolecithins (lysophosphatidylethanolamines and lysophosphatidylcholines - LPC) along with increased lecithins (phosphatidylethanolamines, phosphatidylglycerol and phosphatidylcholines - PC) when we compared ProgMS chronic lesion core vs. CWM (**Fig. 4g,h**). Lysophosphatidylcholines - LPC and phosphatidylcholines – PC are the identical lipids that we observed in the blood (**Fig. 2**). Heatmap visualization of these metabolites across tissues demonstrated that the CA edge exhibited a similar metabolic profile as the lesion core (**Fig. 4h**). Taken together, these results show that ProgMS chronic lesions accumulate PCs and other lecithins through altered Lands cycle, the same metabolic modification seen in blood ProgMS classical monocytes (**Fig. 2**).

Remyelinating lesions have a similar lipidomic profile as CWM and NAWM

We then asked whether the lipid metabolism changes we observed were associated with remyelination in the CNS. To address this, we analyzed a rich dataset that included transcriptomic (bulk RNAseq) and lipidomic profiles of CWM, NAWM, CA, mixed chronic active and inactive lesions (CM), CI and RL samples (*9*). Principal component analysis (PCA) of the transcriptomic landscape of the different tissue types showed a clear separation of tissue without lesions (CWM and NAWM) from tissue with lesions (CA, CM, CI and RL) (**Fig. 5a**). Differential expression analysis showed upregulation of ferroptosis markers (*FLVCR2, SLC7A11, SLC39A8, TMEM164, STEAP3, GCLM* and *GSTK1*) and peroxisome activity genes (*PRDX5, KLF4, KDM6B, DUSP1, RAC2, CLEC7A*

and *CYP1B1*) in all tissues with lesions compared to tissues without lesions (**Fig. 5b**). Moreover, foam cells markers (*SDC2, SDC4, LPCAT1, NLRP3, TSPOAP1* and *B3GNT5*) were increased in CA, CM, CI and RL vs. CWM and NAWM (**Fig. 5b-d**). Of note, *LPCAT1* was downregulated in RL compared to CI and CM (p = 0.041 and 0.0015) and showed a trend for RL vs. CA (p= 0.15) (**Fig. 5c**). We did not observe this pattern for *SDC2* (**Fig. 5d**). We then analyzed the lipidomic data from the same samples. Lipidomics PCA analysis showed that CWM and NAWM samples grouped closely, whereas CA, CM and CI were distant from tissue samples without lesions (**Fig. 5e**). Most of the RL samples in the PCA projection were located around CWM and NAWM (**Fig. 5e**). When we compared CI vs. CWM, we found a reduction in LPCs and an increase in PCs in CI (**Fig. 5f**), which is consistent with the previous metabolomics analysis (**Fig. 4g,h**) and which corroborates the Lands cycle deregulation through LPCAT1. We then analyzed the levels of LPCs and PCs and found that CI, CA and CM shared a signature consisting of decreased LPC and increased PC, whereas RL had a signature consisting of decreased PC and increased LPC, a signature shared with CWM and NAWM (**Fig. 5g**). These results indicate that remyelinating lesions have a less pathogenic Lands cycle profile that they acquire through downregulating *LPCAT1*.

Subpial lesions have increased *SDC2*+ foam cells with similar transcriptional profile as chronic white matter lesions

Subpial lesions are cortical grey matter lesions that form in the outermost layers of the cerebral cortex. They are driven by diffuse, "smoldering" inflammation within the meninges (*32*). Studies utilizing ultra-high field 7 Tesla MRI show that subpial lesion load strongly correlates with progressive disease and irreversible disability (*33, 34*). We thus investigated foam cells in an MS grey matter public omics dataset, focusing on subpial lesions. We analyzed a postmortem human brain snRNA-seq (GEO accession code GSE277430) consisting of CWM, control grey matter (CGM), MS normal appearing grey matter (NAGM) and subpial lesion samples (*35*). We characterized the distinct cell types and plotted them in an UMAP projection split by group and found increased foam cells in the subpial group compared to other three groups (**Fig. 6a**). The foam cells we identified had the identical transcriptomic signature we found in foam cells from white matter chronic lesions and peripheral foam-like cells, including high expression of *SDC2* (**Fig. 1f, 4b and 6b**). When we analyzed the expression of Lands cycle related genes, we found that the subpial foam cells had downregulation of *PLA2G4A* and upregulation of

LPCAT1 compared to other brain myeloid cells (**Fig. 6c**). Furthermore, the subpial foam cells exhibited increased expression of ferroptosis related genes and had a peroxisome activity transcriptional signature that was not seen in other brain myeloid cells (**Fig. 6d,e**). These results indicate that subpial foam cells undergo the same lipidic modulation and cellular stress characterized in CA/CI foam cells and peripheral foam cells. We then analyzed the spatial distribution of *SDC2*+*LPCAT1*+ spots in the spRNA-seq dataset grey matter samples from the cohort analyzed in **Fig. 4**. CGM images had a low number of *SDC2*+*LPCAT1*+ spots, NAGM had a slightly higher number, and subpial lesions exhibited the highest number of *SDC2*+*LPCAT1*+ spots, especially located in demyelinated regions (**Fig. 6f**). Differential expression analysis of *SDC2* in the spRNA-seq data showed increased expression in subpial lesions vs. CGM and NAGM (**Fig. 6g**). *LPCAT1* expression was increased in both subpial and NAGM compared to CGM (**Fig. 6h**). In addition, we analyzed a postmortem human brain proteome (ProteomeXchange Consortium accession code PXD026529) performed from CGM, NAGM and subpial lesion samples (*36*). SDC2 was increased in subpial vs. NAGM and CGM (**Extended Data Fig. 4a,b**). The pathway enrichment analysis of upregulated differentially expressed proteins (DEPs) in subpial vs. NAGM identified several pathways related to phospholipid metabolism and syndecan interactions (**Extended Data Fig. 4c**). These findings indicate that *SDC2*+ foam cells also play a role in subpial lesions with increased ferroptosis and peroxisome activity and are increased in demyelinated grey matter. Finally, we asked whether there was a correlation between *SDC2* expression in peripheral classical monocytes and subpial lesions as measured by 7T MRI. For this, we studied subjects from the CLIMB longitudinal cohort study at our MS Center who had RNAseq analysis of blood monocytes and 7T MRI (n =18). We found that *SDC2* gene expression correlated both with subpial number and subpial volume (**Fig. 6i,j**).

DISCUSSION

In this study, we identified a previously unrecognized SDC2+ foam-like cell subpopulation in circulating classical monocytes from patients with progressive multiple sclerosis and show that its abundance is associated with disability worsening independent of relapse activity. By combining single-cell transcriptomics, flow cytometry, untargeted lipidomics, and reanalysis of public CNS datasets, we provide evidence that these cells are not only enriched in ProgMS and during PIRA events but also share a highly conserved transcriptional and metabolic

signature with foam cells present in chronic active and subpial lesions. Together, these findings support the existence of a systemic myeloid program linked to chronic, relapse-independent progression in MS.

A key observation from our study is that SDC2+ foam-like cells are selectively enriched in ProgMS classical monocytes and increase further during PIRA. Their frequency correlated positively with EDSS, and in one longitudinally sampled patient, the proportion of these cells rose markedly over four years in parallel with worsening disability. This temporal association suggests that the emergence of this monocyte state may reflect ongoing biological progression rather than transient inflammatory activity.

The transcriptional features of foam-like cells suggest that they represent a distinct monocyte state with both inflammatory and lipid-handling properties. These cells not only expressed canonical inflammatory genes, but also markers strongly associated with lipid uptake, syndecan biology, and metabolic remodeling, including SDC2 and SDC4. The selective upregulation of SDC2 was particularly notable, given its validation at the protein level and its strong association with EDSS. Syndecans are known to participate in lipid uptake and membrane organization (*17-19*), and their expression here may indicate a role in lipid internalization and foam cell-like differentiation. This phenotype is consistent with the concept that myeloid cells in progressive MS adopt a metabolically specialized state that supports chronic tissue injury (*9, 37, 38*).

Lipidomics analysis revealed that ProgMS classical monocytes accumulate phosphatidylcholines while exhibiting reduced lysophosphatidylcholine levels, pointing to altered phospholipid remodeling through the Lands cycle. The coordinated upregulation of *LPCAT1* and downregulation of *PLA2G4A* strongly supports increased reacylation of LPC into PC and reduced phospholipid hydrolysis. This pattern was observed not only in ProgMS classical monocytes, but also in foam-like cells and in PIRA samples, suggesting that Lands cycle dysregulation is a constant feature of this disease-associated monocyte state. The concomitant reduction in circulating LPC and arachidonate further supports a model in which peripheral monocytes acquire lipids from serum and channel them toward phosphatidylcholine synthesis. This metabolic shift may contribute to foam cell formation and may also alter membrane composition, signaling, and inflammatory responsiveness.

Our data suggests a close relationship between the lipid-remodeling state of these cells and activation of oxidative stress and ferroptosis-associated programs. ProgMS and PIRA monocytes showed enrichment of peroxisome-related and ferroptosis-related pathways, together with increased expression of genes involved in

iron handling, redox balance, and oxidative stress responses. This is consistent with a foam cell phenotype, as lipid accumulation, oxidative stress, and iron metabolism are closely intertwined (*13, 14, 16*). The observed upregulation of *GPX4* and other ferroptosis-associated genes may indicate a compensatory response to lipid peroxidation stress, rather than protection from ferroptotic cell death. In this context, blood foam-like cells may represent a metabolically stressed monocyte state poised for dysfunction, persistence, or differentiation into tissue-infiltrating inflammatory macrophages.

The parallel findings in chronic CNS lesions strongly reinforce the relevance of these peripheral observations. Reanalysis of public snRNA-seq datasets revealed increased foam cell populations in chronic active/inactive white matter lesions, all expressing the same *SDC2*-high signature found in peripheral foam-like cells. These lesion-resident foam cells also showed elevated *LPCAT1* and reduced *PLA2G4A*, mirroring the peripheral Lands cycle signature. Moreover, lesion metabolomics demonstrated reduced LPCs and increased PCs, consistent with altered phospholipid remodeling. This concordance between peripheral blood and CNS tissue suggests that the same lipid-driven program operates across anatomical compartments, potentially linking circulating monocyte states to chronic lesion biology.

The association of these cells with chronic lesions and subpial pathology is particularly important for understanding PIRA in subjects with MS. Chronic active lesions and subpial lesions are thought to reflect compartmentalized inflammation and smoldering neurodegeneration that drive progressive MS and PIRA, rather than acute attacks (*26, 27*). The enrichment of *SDC2+* foam cells in these lesion types, along with their shared transcriptional signature with peripheral foam-like cells, suggests that these cells may participate in sustaining chronic lesion activity or may serve as peripheral mirrors of ongoing CNS pathology. The spatial localization of *SDC2+LPCAT1+* spots in demyelinated tissue further supports their involvement in lesion biology. Their presence in subpial lesions is especially notable, given the strong association of these lesions with progressive disability as measured by MRI (*32, 34*).

An additional important finding is that remyelinating lesions appear to partially revert the lipidomic pattern observed in chronic lesions. In remyelinating tissue, *LPCAT1* expression was reduced and lipid profiles shifted closer to control white matter, suggesting that restoration of myelin-associated metabolic homeostasis may involve normalization of the Lands cycle. This observation provides a potential mechanistic link between lesion resolution and lipid remodeling, raising the possibility that phospholipid metabolism may be a marker of lesion

fate and a target of treatment to promote remyelination. Thus, LPCAT1 and related metabolic features may help distinguish lesions that remain chronically active from those that successfully remyelinate.

Our data supports a working model in which SDC2+ classical monocytes from ProgMS patients adopt a lipid-stressed state driven by dysfunctional Lands cycle activity (**Extended Data Fig. 5**). In this model, altered phospholipid remodeling promotes phosphatidylcholine accumulation while reducing lysophosphatidylcholine availability, thereby creating a membrane environment prone to oxidative damage. Concomitantly, increased iron uptake through FLVCR2 may intensify intracellular iron loading, favoring lipid peroxidation and activation of ferroptosis-associated programs. We therefore propose that Lands cycle dysregulation and iron handling converge in SDC2+ classical monocytes to sustain a ferroptosis-prone phenotype that may contribute to disability worsening in progressive MS. Paramagnetic rim lesions (PRLs) provide an in vivo imaging correlate of chronic active MS lesions and are defined by a susceptibility-sensitive MRI rim that reflects iron-enriched, activated microglia and macrophages at the lesion edge (*39, 40*). The enrichment of iron-handling and ferroptosis-associated transcripts in SDC2+ foam cells described here raises the possibility that this lipid-stressed myeloid program is mechanistically related to PRL biology. In particular, altered phospholipid remodeling and phosphatidylcholine accumulation could increase the pool of oxidation-susceptible membrane lipids, while increased iron uptake and dysregulated redox responses may promote lipid peroxidation at the chronic lesion edge. Consistent with this model, MS lesions have been reported to contain elevated labile iron, peroxidized phospholipids and lipid-peroxidation products, including within chronic lesion rims populated by foamy myeloid cells (*41*). Thus, PRL burden could be evaluated in future longitudinal cohorts as an imaging readout of the proposed ferroptosis-prone myeloid state and its relationship to circulating SDC2+ monocytes, PIRA and disability accumulation; importantly, the present data supports a biological association rather than direct evidence that peripheral monocytes generate PRL rims.

In summary, our findings identify SDC2+ foam-like cells as a progressive MS-associated monocyte state linked to disability worsening and PIRA. These cells exhibit a distinctive lipid metabolic program centered on the Lands cycle, alongside transcriptional activation of ferroptosis and peroxisome-related pathways. The striking similarity between peripheral foam-like cells and foam cells in chronic CNS lesions suggests a shared myeloid program that may bridge systemic immune alterations and compartmentalized CNS pathology in progressive

MS. Finally, these results identify SDC2, LPCAT1, and related lipid remodeling pathways as potential biomarkers for disease progression in MS and raise the possibility that they could be targets for treatment of MS progression.

MATERIAL AND METHODS

Patient Selection

We included MS patients with i) non-active disease defined by no clinical relapse or MRI changes in two years prior to sampling and ii) untreated defined by being treatment naïve without haven't received steroids for 1 month, interferon or glatiramer acetate for 3 months, natalizumab for 6 months, S1P inhibitors, teriflunomide or dimethyl fumarate for 12 months or anti-CD20 therapy for 18 months. Patients were classified based on their disease course as RRMS and ProgMS according to the most recent 2020 classification by Lublin, *et al* (*42*). We also included healthy controls matched to the patients by age and assigned sex. The patients included in this study were part of the Comprehensive Longitudinal Investigation of MS at the Brigham and Women's Hospital (CLIMB, www.climbstudy.org), a natural history study that encompasses biannual clinical assessment, annual MRI, blood samples (*43*). The biannual clinical assessment includes measurement of the EDSS, SDMT and the timed 25-foot walk. A relapse was recorded by the treating neurologist at onset of new or recurrent MS symptom lasting for ≥ 24h. Institutional Review Board (IRB) approval was granted by the Partners Human Research Committee, and participants provided written informed consent for participation.

Determination of PIRA events

PIRA events were determined for each patient based on longitudinal Expanded Disability Scale (EDSS) scores and clinical attack data following 2025 consensus guidelines (*44*), using a roving baseline to increase sensitivity to events (*44-46*). Briefly, a disability accrual event was defined as a scaled increase from the reference EDSS (+1.5 for EDSS 0, +1.0 for EDSS 1-5, +0.5 for EDSS ≥ 5.5) given non-linearity in the EDSS. Disability accrual was confirmed if the EDSS at a following visit ≥12 months after the incident visit, as well as all intervening visits, met the same increase criteria. A CDA event was called PIRA if there were no relapses between the incident visit and the visit prior, and no relapses in the 30 days before each confirmation score. If there was an increase in the EDSS that met the disability accrual definition with a relapse since the previous visit, a RAW event was called. EDSS scores were initialized using the EDSS at first visit, but re-baselined after a CDA or confirmed

disability improvement (CDI) events (decrease in EDSS score sustained over a follow up visit ≥180 days later). For PIRA and CDI events, the baseline was reset to the EDSS at the confirmation visit. For RAW events, the baseline was reset to the EDSS at a clinical visit >30 days after the relapse. Detection of PIRA events was performed in R.

Myeloid cell isolation

Aliquots of PBMCs samples stored in liquid nitrogen at -140°C were thawed and resuspended in fluorescent activated cell sorting (FACS) buffer: Hank's Balanced Salt Solution Ca-/Mg- (Gibco, Cat# 14175-095) supplemented with 20mM HEPES (Lonza, Cat# 17-737E), 2.5 mM EDTA (Invitrogen, Cat# 15575-038) and 2% Fetal Bovine Serum (Gibco, Cat# A3160501). Cells were spun down at 400g for 5 minutes at 4°C and the supernatant was removed. The cell pellet was resuspended in 100uL of FACS buffer and stained for 15 minutes at room temperature with viability dye eFluor660 (Thermo Fisher Scientific, Cat# 65-0864-14). Residual dye was removed by a wash step, and the cell pellet was resuspended in 1 mL of FACS buffer. This volume was then filtered through a 45µm filter cap and kept on wet ice. Myeloid cells were isolated by FACS sorting on Aria sorter by forward scatter and side scatter, based on their larger cell size compared to lymphocytes (*47*). Dead cells were positive for efluor660 and removed. A 100µm nozzle was used to reduce cell stress. Half a million monocytes were collected for each sample and processed for sequencing.

Myeloid cell sequencing

Myeloid cells were counted manually utilizing a hemocytometer and a volume corresponding to 60,000 cells was loaded in the Chromium Next GEM Chip G Single Cell Kit (10X Genomics, Cat# 1000127). The chip was loaded on a Chromium controller where individual cells are isolated into droplets together with gel beads coated with unique primers bearing 10X cell barcodes, UMI (unique molecular identifiers) and poly(dT) sequences. Reverse transcription reactions allow them to generate barcoded full-length cDNA followed by the disruption of emulsions using the recovery agent and cDNA clean up. Bulk cDNA is amplified and cleaned up. Indexed sequencing libraries will be constructed using the reagents from the Chromium Next GEM Single Cell 3′ Reagent Kits v3.1 (Dual index; 10X Genomics, Cat# 1000268). Indexed libraries were equimolarly pooled and sequenced on an Illumina Novaseq S4 using paired-end 28x90bp as sequencing mode aiming at ≥ 20,000 paired reads per cell and ~20,000 cells per each library.

Single-cell RNA-seq analysis

Illumina fastq files were processed using 10X Genomics Cell Ranger v7.0.1 pipeline, aligning to GRCh38 2020. The count matrixes generated served as input to downstream analysis in Seurat (version 5.1.0) with BPCells implementation for RAM memory usage optimization (*48*). Cells with UMIs over 5,000 or less than 500, and more than 10% mitochondrial counts were filtered out. The feature expression measurements for each cell were normalized by the total expression, multiplied by the scale factor (10,000), and log transformed. We calculated the 1,500 highly variable genes, followed by linear transformation (scaling) regressing out heterogeneity associated with mitochondrial contamination. Linear dimensional reduction was performed by PCA, followed by non-linear UMAP embedding using the first 40 principal components, same parameter as used for clustering with both FindNeighbors and FindClusters (0.5 resolution) Seurat's functions. Residual clusters of non-myeloid cells were filtered out. Differential gene-expression comparison between groups of subjects was conducted through MAST (*49*), using sex and age as covariates. Differential gene-expression comparison between the samples pre and post PIRA from the same subject was conducted through Wilcoxon Rank Sum test. For both comparisons, DEGs were selected based on adjusted *p* value (Bonferroni correction) < 0.05 and detected in a minimum fraction of 10% cells in either of the two populations. Differential gene-expression amongst distinct cell types to identify cell markers was conducted through Wilcoxon Rank Sum test. DEGs were selected based on adjusted *p* value (Bonferroni correction) < 0.05, detected in a minimum fraction of 33% cells and fold-change higher than 1.5 times.

Pathway enrichment analysis

Pathway and gene ontology analysis were conducted through Over-Representation Analysis (ORA), splitting downregulated from upregulated genes, using the following databases: Enrichr-KG (*50-52*), PANTHER 19.0 (*53*), and WebGestalt (*54*). Pathways were considered enriched based on adjusted *p* value (Bonferroni correction) < 0.05.

Public postmortem brain snRNA-seq datasets analyses

Initially we obtained the count matrices from a public database (Gene Expression Omnibus - GEO). These count matrices served as input to downstream analysis in Seurat (version 5.1.0) (*48*). Cells with UMIs over 5,000 or less than 500, and more than 5% mitochondrial counts were filtered out. The feature expression was normalized

and scaled as standard recommendations. We calculated the 3,000 highly variable genes modeling the mean-variance. Dimensional reduction was performed by UMAP using the first 40 principal components, and FindClusters with a resolution of 1.5. Cell types were assigned using well-known gene markers for CNS and immune cells. Differential gene-expression comparison between groups (tissue types) was conducted through MAST (*49*), using sex and age as covariates. Differential gene-expression amongst distinct cell types was conducted through Wilcoxon Rank Sum test.

Public postmortem brain bulk RNAseq analysis

The count matrix obtained from GEO was direct to differential analysis with DESeq2 (version 1.48.1) R 4.5 package (*55*) with sex and age as covariates. The Cook's distance together with Principal components analysis and hierarchical clustering of the 1000 most variable genes were used to identify outliers.

Flow Cytometry

A total of 1 × 10^6 cells of peripheral blood mononuclear cells (PBMCs) were thawed in pre-warmed complete IMDM medium and left unstimulated. Next, cells were processed for multiparameter flow cytometric analysis. For viability assessment, cells were stained with Zombie Aqua viability dye (1:1,000 dilution) using a final staining volume of 50 µL per sample. Samples were incubated for 15 min at room temperature and subsequently washed by centrifugation at 600 × g for 3 min at 4°C. Surface staining was performed in a final volume of 50 µL per sample using the following fluorochrome-conjugated antibodies: CD45-PE-Cy7 (BioLegend, cat. no. 368531), CD20-AF700 (BioLegend, cat. no. 375523), CD56-AF700 (BioLegend, cat. no. 318315), CD3-BV711 (BioLegend, cat. no. 300463), CD14-APC-Cy7 (BioLegend, cat. no. 325619), CD16-BV605 (BioLegend, cat. no. 302039), CD362-AF647 (Santa Cruz Biotechnology, cat. no. 365624), TCRβ-PerCP-Cy5.5 (BioLegend, cat. no. 306723). CD3 and TCRβ were included as dump-channel markers to facilitate the exclusion of T cells. CD20 and CD56 were included as dump-channel markers to facilitate the exclusion of B cells and NK cells, respectively. Unless otherwise specified, antibodies were used at a 1:100 dilution. Surface antibody staining was performed for 30 min at 4°C. Samples were subsequently washed by centrifugation at 600 × g for 3 min at 4°C. Data were acquired using an Aurora spectral flow cytometer (Cytek Biosciences). Data were analyzed using a sequential gating strategy. Events were first gated on the leukocyte population by forward- and side-scatter characteristics to exclude debris, followed by doublet discrimination using forward-scatter area versus height (or width) parameters. Live cells were identified as Zombie Aqua–negative events and gated for CD45 expression. Within

live CD45+ singlets, T cells, B cells, and NK cells were excluded using a dump gate comprising CD3/TCRβ, CD20, and CD56, respectively. Monocytes were subsequently identified on the basis of CD14 and CD16 expression, and CD362 expression was quantified as the frequency of CD362+ cells and/or median fluorescence intensity within the indicated monocyte population. The CD362-positive gate was established using a fluorescence-minus-one (FMO) control containing the complete antibody panel except anti-CD362–AF647, thereby accounting for fluorescence spread and background signal in the CD362 channel; identical gate boundaries were applied across all samples. FMO controls are particularly appropriate for defining low or continuous marker expression in multicolor flow cytometry.

Classical monocytes lipidomics

To determine the relative abundance of lipids, extracts were prepared and analyzed by C30 chromatography-mass spectrometry (C30-MS). Lipids were extracted using ice-cold 100 µM butylated hydroxytoluene in ethanol containing 2% Avanti SPLASH® LIPIDOMIX® Mass Spec Standard. Extracts were centrifuged at 17,000 g for 5 min at 4°C, and supernatants were evaporated to dryness under nitrogen. Dried extracts were reconstituted in 200 µL ethanol, and 10 µL was injected for analysis. Mobile phase A (MPA; weak) was 0.1% formic acid and 10 mM ammonium formate in acetonitrile:water = 40:60. Mobile phase B (MPB; strong) was 0.1% formic acid and 10 mM ammonium formate in isopropanol:acetonitrile:water = 90:9:1. A Thermo Dionex Vanquish LC system included an Accucore C30 column (2.6 µm, 150 x 2.1 mm) with column compartment set at 40°C. The autosampler tray was chilled to 8°C. The mobile phase flow rate was 200 µL/min, and the gradient elution program was: 0-3 min, 30% MPB; 3-13 min, 30-43% MPB; 13.1-33 min, 50-70% MPB; 33-48 min, 70-99% MPB; 48-55 min, 99% MPB; 55.1-60 min, 30% MPB. The total run time was 60 min. Data were acquired using a Thermo Fisher Scientific Orbitrap Fusion Lumos Tribrid mass spectrometer under ESI positive and negative ionization modes with data dependent acquisition, scan ranges from 150 –1500 m/z, resolution of 240,000 for MS1 acquisition, and spray voltages of 3,600 and -2900 V for positive and negative ionization modes, respectively. Vaporizer and ion transfer tube temperatures were set at 275°C and 300°C, respectively. The sheath, auxiliary and sweep gas pressures were 35, 10, and 0 (arbitrary units), respectively. A hybrid CID/HCD approach was used for MS2 and MS3 fragmentation.

Lipidomics, metabolomics and proteomics analysis

The relative abundance (mass spectrometry peak area) of each metabolite/peptide was initially normalized by z-score normalization. Metabolites/peptides with too many missing values (>40%) were filtered out, then random forest imputation was applied followed by LOWESS smoothing with a moving average of 40. Finally, we performed ANCOVA with gender and age as covariates.

Public postmortem brain Spatial RNAseq analyses

We obtained the 10X Visium count matrices and image files from a public database (Gene Expression Omnibus - GEO). These files served as input to downstream analysis in Seurat (version 5.1.0) (*48*). The feature expression was normalized and scaled as standard recommendations. We calculated the 3,000 highly variable genes modeling the mean-variance. Dimensional reduction was performed by UMAP using the first 30 principal components, and FindClusters with a resolution of 2. Cell types were assigned to spots using well-known gene markers for CNS and immune cells. Differential gene-expression comparison between groups (tissue types) was conducted through MAST (*49*), using sex and age as covariates. Differential gene-expression amongst distinct cell types was conducted through Wilcoxon Rank Sum test.

Statistical analysis

For normally distributed data, we used one way-ANOVA (followed by Tukey-Kramer test for multiple comparisons) and considered it statistically different when $p<0.05$. For multi-group comparison of data that does not meet normal distribution, we performed Kruskal-Wallis test, considering it statistically different when $p<0.05$. Robust nonlinear regression was used for outlier removal, with coefficient Q equals 1%. Pearson correlation was conducted for linear regression of homoscedastic data, and Spearman was used for heteroscedastic data.

Data and code availability

The single-cell RNA-seq raw data presented in this work is publicly available at the NCBI's BioProject with the following accession code PRJNA1234700. The classical monocytes lipidomics data is publicly available at Zenodo (https://doi.org/10.5281/zenodo.23173299). All code for data processing and analysis is available at GitHub (https://github.com/tobylanser/sc_MS_monocyte_scripts). This work also analyzed publicly available data, which can be accessed through Gene Expression Omnibus (GSE144744, GSE208747, GSE277430), GitHub repository (github.com/dladakis/ms_tissue_metabolomics), NCBI BioProject (PRJNA544731),

ProteomeXchange Consortium (accession code PXD026529) and Zenodo (https://doi.org/10.5281/zenodo.17735822).

Conflicts of Interest

Authors declare no conflict of interest.

Author's Contributions

P.S. analyzed the scRNA-seq, lipidomics and spRNA-seq data, created the hypothesis, and wrote the manuscript. M.G.O., M.P.T., S.S., T.Y. and M.H.A.M. handled samples and performed validation experiments. R.S.F. and T.L. analyzed the single cell RNA sequencing data. F.M., J.Z. and S.M. performed bulk RNAseq of classical monocytes and assessed subpial lesions through 7T MRI of ProgMS patients. J.Y. and B.C.H. identified PIRA events in patients' records. M.K. and C.B. selected patients, designed and performed the sequencing. H.L.W., T.C., R.M.R, S.I. and L.C. supervised the project.

Fig. 1

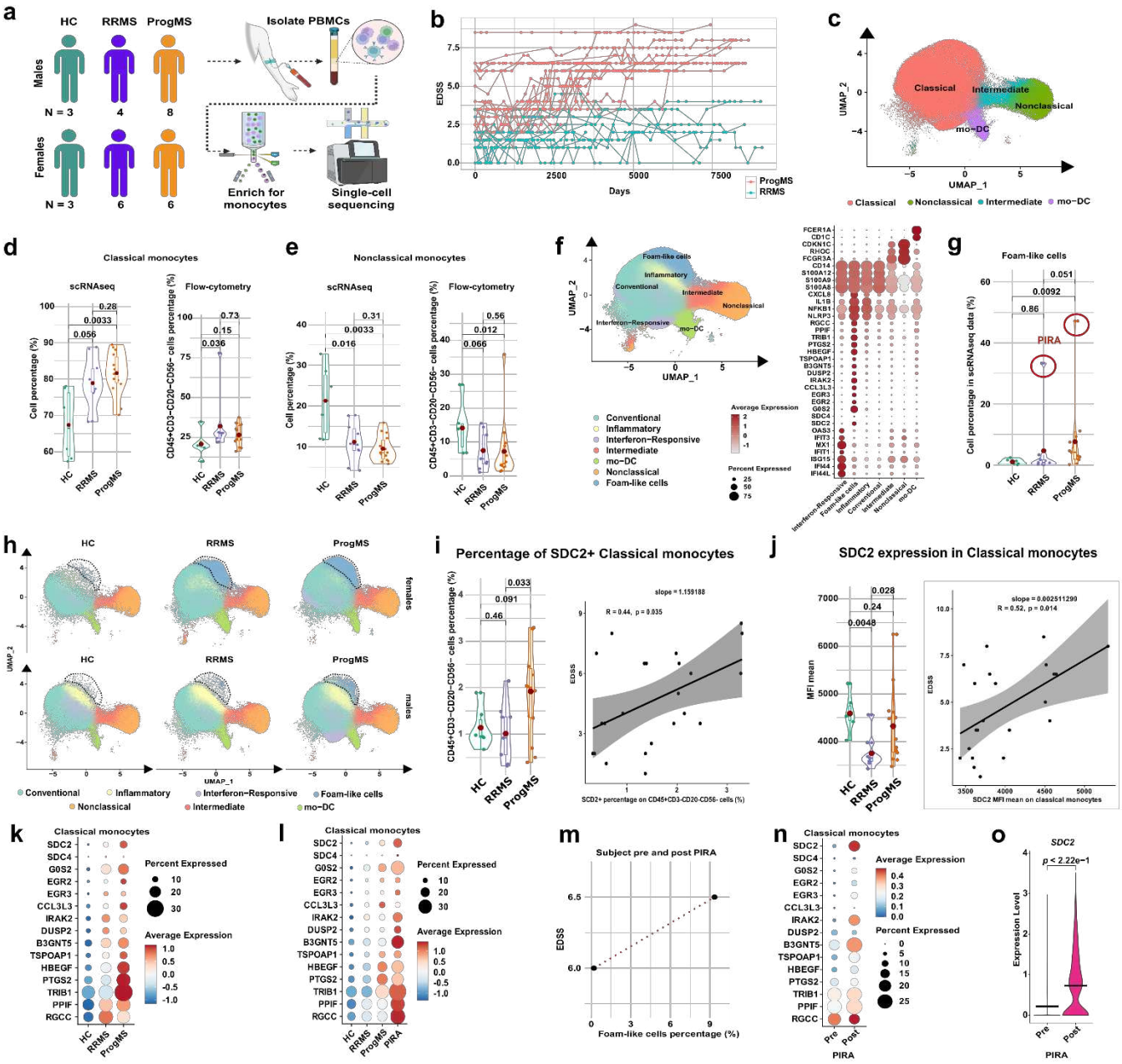

a
HC
RRMS
ProgMS
Males
Females
N = 3
4
8
6
6
Isolate PBMCs
Enrich for monocytes
Single-cell sequencing
b
EDSS
Days
ProgMS
RRMS
c
UMAP_2
UMAP_1
Classical
Intermediate
Nonclassical
mo−DC
d
Classical monocytes
scRNAseq
Flow-cytometry
Cell percentage (%)
CD45+CD3−CD20−CD56− cells percentage (%)
e
Nonclassical monocytes
f
Foam-like cells
Inflammatory
Conventional
Intermediate
Nonclassical
Interferon−Responsive
mo−DC
Average Expression
Percent Expressed
g
Foam-like cells
Cell percentage in scRNAseq data (%)
PIRA
h
HC
RRMS
ProgMS
females
males
Conventional
Inflammatory
Interferon−Responsive
Foam-like cells
Nonclassical
Intermediate
mo−DC
i
Percentage of SDC2+ Classical monocytes
CD45+CD3−CD20−CD56− cells percentage (%)
SCD2+ percentage on CD45+CD3-CD20-CD56- cells (%)
j
SDC2 expression in Classical monocytes
MFI mean
SDC2 MFI mean on classical monocytes
k
Classical monocytes
Percent Expressed
Average Expression
l
Classical monocytes
m
Subject pre and post PIRA
Foam-like cells percentage (%)
n
Classical monocytes
Average Expression
Percent Expressed
PIRA
o
SDC2
Expression Level
PIRA

Fig. 2

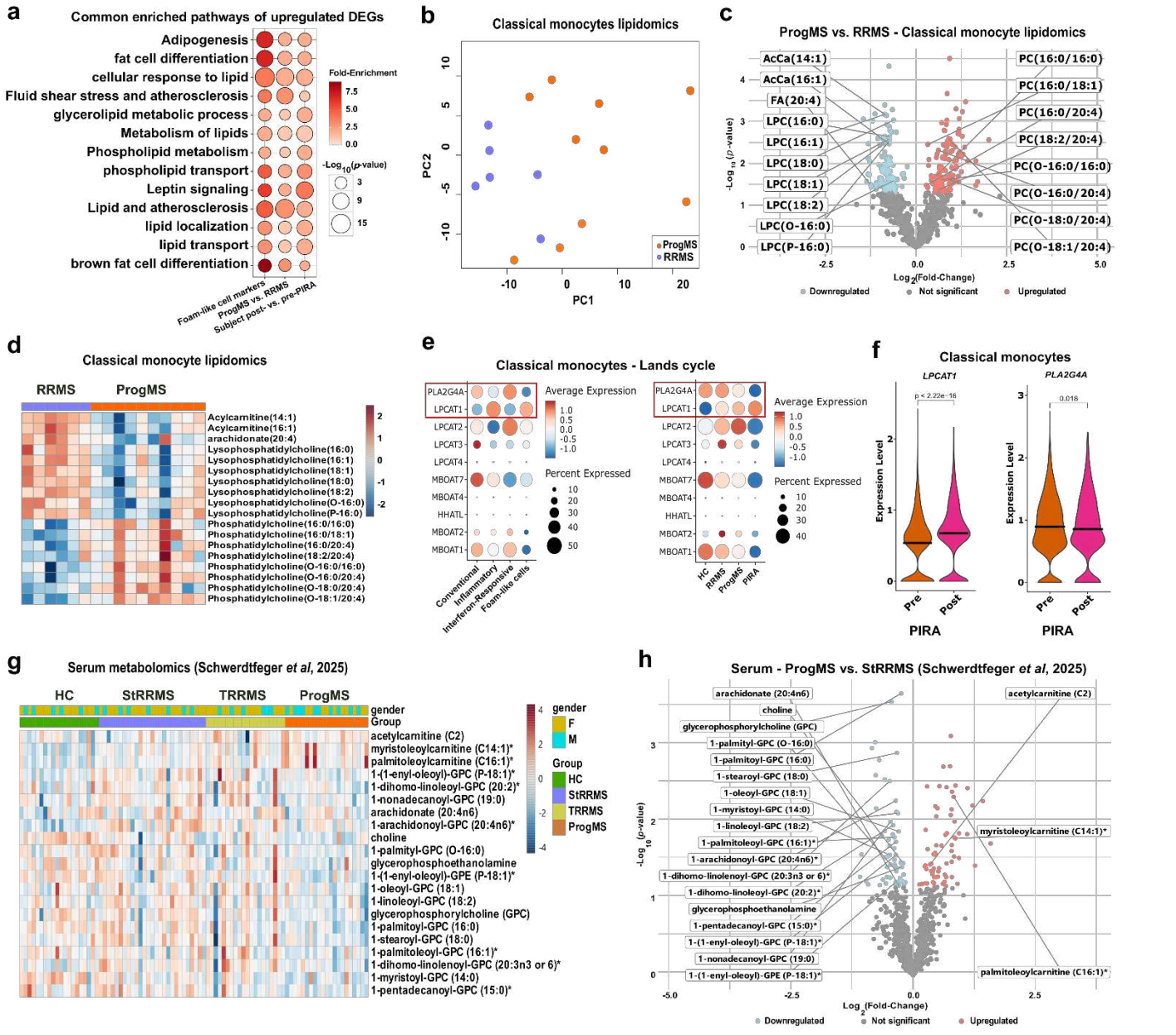

a
Common enriched pathways of upregulated DEGs
Adipogenesis
fat cell differentiation
cellular response to lipid
Fluid shear stress and atherosclerosis
glycerolipid metabolic process
Metabolism of lipids
Phospholipid metabolism
phospholipid transport
Leptin signaling
Lipid and atherosclerosis
lipid localization
lipid transport
brown fat cell differentiation
Foam-like cell markers
ProgMS vs. RRMS
Subject post- vs. pre-PIRA
Fold-Enrichment
-Log10(p-value)
b
Classical monocytes lipidomics
PC1
PC2
ProgMS
RRMS
c
ProgMS vs. RRMS - Classical monocyte lipidomics
AcCa(14:1)
AcCa(16:1)
FA(20:4)
LPC(16:0)
LPC(16:1)
LPC(18:0)
LPC(18:1)
LPC(18:2)
LPC(O-16:0)
LPC(P-16:0)
PC(16:0/16:0)
PC(16:0/18:1)
PC(16:0/20:4)
PC(18:2/20:4)
PC(O-16:0/16:0)
PC(O-16:0/20:4)
PC(O-18:0/20:4)
PC(O-18:1/20:4)
-Log10 (p-value)
Log2(Fold-Change)
Downregulated
Not significant
Upregulated
d
Classical monocyte lipidomics
RRMS
ProgMS
Acylcarnitine(14:1)
Acylcarnitine(16:1)
arachidonate(20:4)
Lysophosphatidylcholine(16:0)
Lysophosphatidylcholine(16:1)
Lysophosphatidylcholine(18:1)
Lysophosphatidylcholine(18:0)
Lysophosphatidylcholine(18:2)
Lysophosphatidylcholine(O-16:0)
Lysophosphatidylcholine(P-16:0)
Phosphatidylcholine(16:0/16:0)
Phosphatidylcholine(16:0/18:1)
Phosphatidylcholine(16:0/20:4)
Phosphatidylcholine(18:2/20:4)
Phosphatidylcholine(O-16:0/16:0)
Phosphatidylcholine(O-16:0/20:4)
Phosphatidylcholine(O-18:0/20:4)
Phosphatidylcholine(O-18:1/20:4)
e
Classical monocytes - Lands cycle
PLA2G4A
LPCAT1
LPCAT2
LPCAT3
LPCAT4
MBOAT7
MBOAT4
HHATL
MBOAT2
MBOAT1
Average Expression
Percent Expressed
Conventional
Inflammatory
Interferon-Responsive
Foam-like cells
HC
RRMS
ProgMS
PIRA
f
Classical monocytes
LPCAT1
PLA2G4A
p < 2.22e-16
0.018
Expression Level
Pre
Post
PIRA
g
Serum metabolomics (Schwerdtfeger et al, 2025)
HC
StRRMS
TRRMS
ProgMS
gender
Group
acetylcarnitine (C2)
myristoleoylcarnitine (C14:1)*
palmitoleoylcarnitine (C16:1)*
1-(1-enyl-oleoyl)-GPC (P-18:1)*
1-dihomo-linoleoyl-GPC (20:2)*
1-nonadecanoyl-GPC (19:0)
arachidonate (20:4n6)
1-arachidonoyl-GPC (20:4n6)*
choline
1-palmityl-GPC (O-16:0)
glycerophosphoethanolamine
1-(1-enyl-oleoyl)-GPE (P-18:1)*
1-oleoyl-GPC (18:1)
1-linoleoyl-GPC (18:2)
glycerophosphorylcholine (GPC)
1-palmitoyl-GPC (16:0)
1-stearoyl-GPC (18:0)
1-palmitoleoyl-GPC (16:1)*
1-dihomo-linolenoyl-GPC (20:3n3 or 6)*
1-myristoyl-GPC (14:0)
1-pentadecanoyl-GPC (15:0)*
F
M
HC
StRRMS
TRRMS
ProgMS
h
Serum - ProgMS vs. StRRMS (Schwerdtfeger et al, 2025)
arachidonate (20:4n6)
choline
glycerophosphorylcholine (GPC)
1-palmityl-GPC (O-16:0)
1-palmitoyl-GPC (16:0)
1-stearoyl-GPC (18:0)
1-oleoyl-GPC (18:1)
1-myristoyl-GPC (14:0)
1-linoleoyl-GPC (18:2)
1-palmitoleoyl-GPC (16:1)*
1-arachidonoyl-GPC (20:4n6)*
1-dihomo-linolenoyl-GPC (20:3n3 or 6)*
1-dihomo-linoleoyl-GPC (20:2)*
glycerophosphoethanolamine
1-pentadecanoyl-GPC (15:0)*
1-(1-enyl-oleoyl)-GPC (P-18:1)*
1-nonadecanoyl-GPC (19:0)
1-(1-enyl-oleoyl)-GPE (P-18:1)*
acetylcarnitine (C2)
myristoleoylcarnitine (C14:1)*
palmitoleoylcarnitine (C16:1)*
-Log10 (p-value)
Log2(Fold-Change)
Downregulated
Not significant
Upregulated

Fig. 3

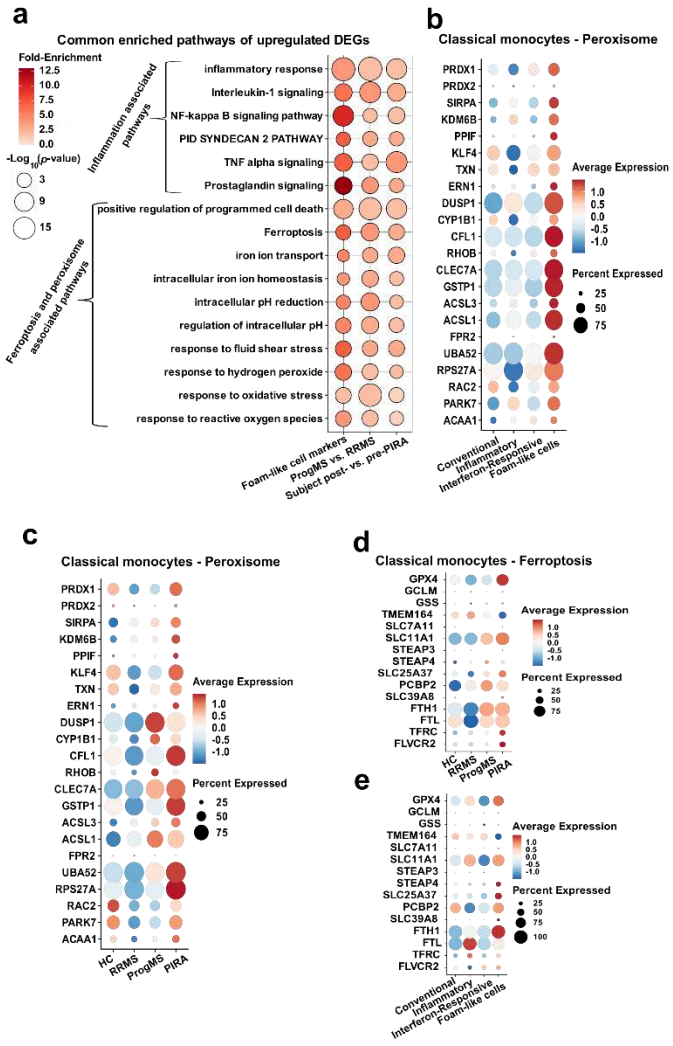

a
Common enriched pathways of upregulated DEGs
Fold-Enrichment
12.5
10.0
7.5
5.0
2.5
0.0
-Log10(p-value)
3
9
15
Inflammation associated pathways
inflammatory response
Interleukin-1 signaling
NF-kappa B signaling pathway
PID SYNDECAN 2 PATHWAY
TNF alpha signaling
Prostaglandin signaling
Ferroptosis and peroxisome associated pathways
positive regulation of programmed cell death
Ferroptosis
iron ion transport
intracellular iron ion homeostasis
intracellular pH reduction
regulation of intracellular pH
response to fluid shear stress
response to hydrogen peroxide
response to oxidative stress
response to reactive oxygen species
Foam-like cell markers
ProgMS vs. RRMS
Subject post- vs. pre-PIRA
b
Classical monocytes - Peroxisome
PRDX1
PRDX2
SIRPA
KDM6B
PPIF
KLF4
TXN
ERN1
DUSP1
CYP1B1
CFL1
RHOB
CLEC7A
GSTP1
ACSL3
ACSL1
FPR2
UBA52
RPS27A
RAC2
PARK7
ACAA1
Average Expression
1.0
0.5
0.0
-0.5
-1.0
Percent Expressed
25
50
75
Conventional
Inflammatory
Interferon-Responsive
Foam-like cells
c
Classical monocytes - Peroxisome
PRDX1
PRDX2
SIRPA
KDM6B
PPIF
KLF4
TXN
ERN1
DUSP1
CYP1B1
CFL1
RHOB
CLEC7A
GSTP1
ACSL3
ACSL1
FPR2
UBA52
RPS27A
RAC2
PARK7
ACAA1
Average Expression
1.0
0.5
0.0
-0.5
-1.0
Percent Expressed
25
50
75
HC
RRMS
ProgMS
PIRA
d
Classical monocytes - Ferroptosis
GPX4
GCLM
GSS
TMEM164
SLC7A11
SLC11A1
STEAP3
STEAP4
SLC25A37
PCBP2
SLC39A8
FTH1
FTL
TFRC
FLVCR2
Average Expression
1.0
0.5
0.0
-0.5
-1.0
Percent Expressed
25
50
75
HC
RRMS
ProgMS
PIRA
e
GPX4
GCLM
GSS
TMEM164
SLC7A11
SLC11A1
STEAP3
STEAP4
SLC25A37
PCBP2
SLC39A8
FTH1
FTL
TFRC
FLVCR2
Average Expression
1.0
0.5
0.0
-0.5
-1.0
Percent Expressed
25
50
75
100
Conventional
Inflammatory
Interferon-Responsive
Foam-like cells

Fig. 4

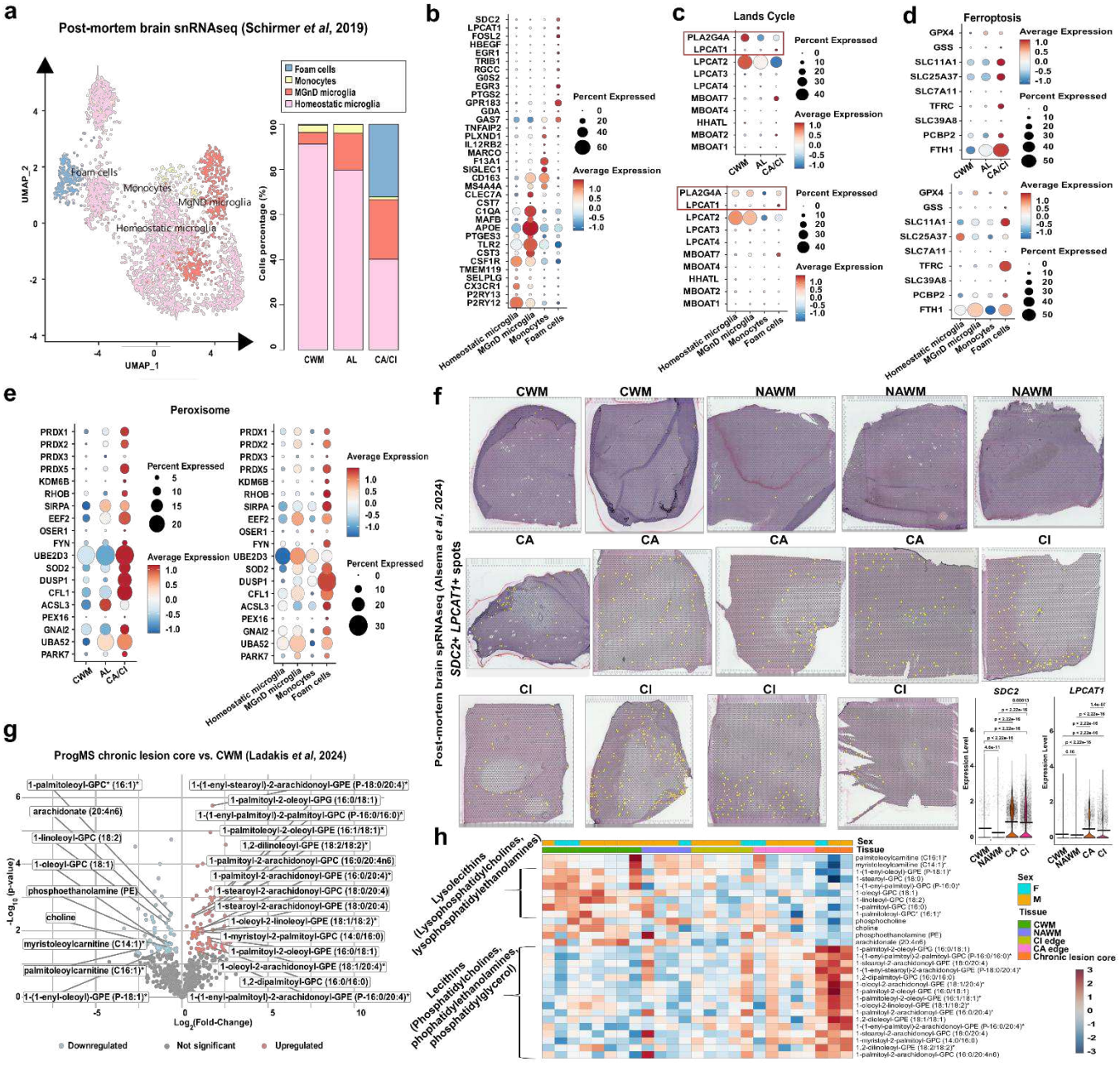

a
Post-mortem brain snRNAseq (Schirmer et al, 2019)
Foam cells
Monocytes
MGnD microglia
Homeostatic microglia
UMAP_1
UMAP_2
Cells percentage (%)
CWM
AL
CA/CI
b
Percent Expressed
Average Expression
Homeostatic microglia
MGnD microglia
Monocytes
Foam cells
c
Lands Cycle
PLA2G4A
LPCAT1
LPCAT2
LPCAT3
LPCAT4
MBOAT7
MBOAT4
HHATL
MBOAT2
MBOAT1
d
Ferroptosis
GPX4
GSS
SLC11A1
SLC25A37
SLC7A11
TFRC
SLC39A8
PCBP2
FTH1
e
Peroxisome
PRDX1
PRDX2
PRDX3
PRDX5
KDM6B
RHOB
SIRPA
EEF2
OSER1
FYN
UBE2D3
SOD2
DUSP1
CFL1
ACSL3
PEX16
GNAI2
UBA52
PARK7
f
Post-mortem brain spRNAseq (Alsema et al, 2024)
SDC2+ LPCAT1+ spots
CWM
NAWM
CA
CI
SDC2
LPCAT1
Expression Level
g
ProgMS chronic lesion core vs. CWM (Ladakis et al, 2024)
1-palmitoleoyl-GPC* (16:1)*
arachidonate (20:4n6)
1-linoleoyl-GPC (18:2)
1-oleoyl-GPC (18:1)
phosphoethanolamine (PE)
choline
myristoleoylcarnitine (C14:1)*
palmitoleoylcarnitine (C16:1)*
1-(1-enyl-oleoyl)-GPE (P-18:1)*
1-(1-enyl-stearoyl)-2-arachidonoyl-GPE (P-18:0/20:4)*
1-palmitoyl-2-oleoyl-GPG (16:0/18:1)
1-(1-enyl-palmitoyl)-2-palmitoyl-GPC (P-16:0/16:0)*
1-palmitoleoyl-2-oleoyl-GPE (16:1/18:1)*
1,2-dilinoleoyl-GPE (18:2/18:2)*
1-palmitoyl-2-arachidonoyl-GPC (16:0/20:4n6)
1-palmitoyl-2-arachidonoyl-GPE (16:0/20:4)*
1-stearoyl-2-arachidonoyl-GPC (18:0/20:4)
1-stearoyl-2-arachidonoyl-GPE (18:0/20:4)
1-oleoyl-2-linoleoyl-GPE (18:1/18:2)*
1-myristoyl-2-palmitoyl-GPC (14:0/16:0)
1-palmitoyl-2-oleoyl-GPE (16:0/18:1)
1-oleoyl-2-arachidonoyl-GPE (18:1/20:4)*
1,2-dipalmitoyl-GPC (16:0/16:0)
1-(1-enyl-palmitoyl)-2-arachidonoyl-GPE (P-16:0/20:4)*
-Log10 (p-value)
Log2(Fold-Change)
Downregulated
Not significant
Upregulated
h
Lysolecithins (Lysophosphatidylcholines, lysophosphatidylethanolamines)
Lecithins (Phosphatidylcholines, phosphatidylethanolamines, phosphatidylglycerol)
Sex
Tissue
F
M
CWM
NAWM
CI edge
CA edge
Chronic lesion core

Fig. 5

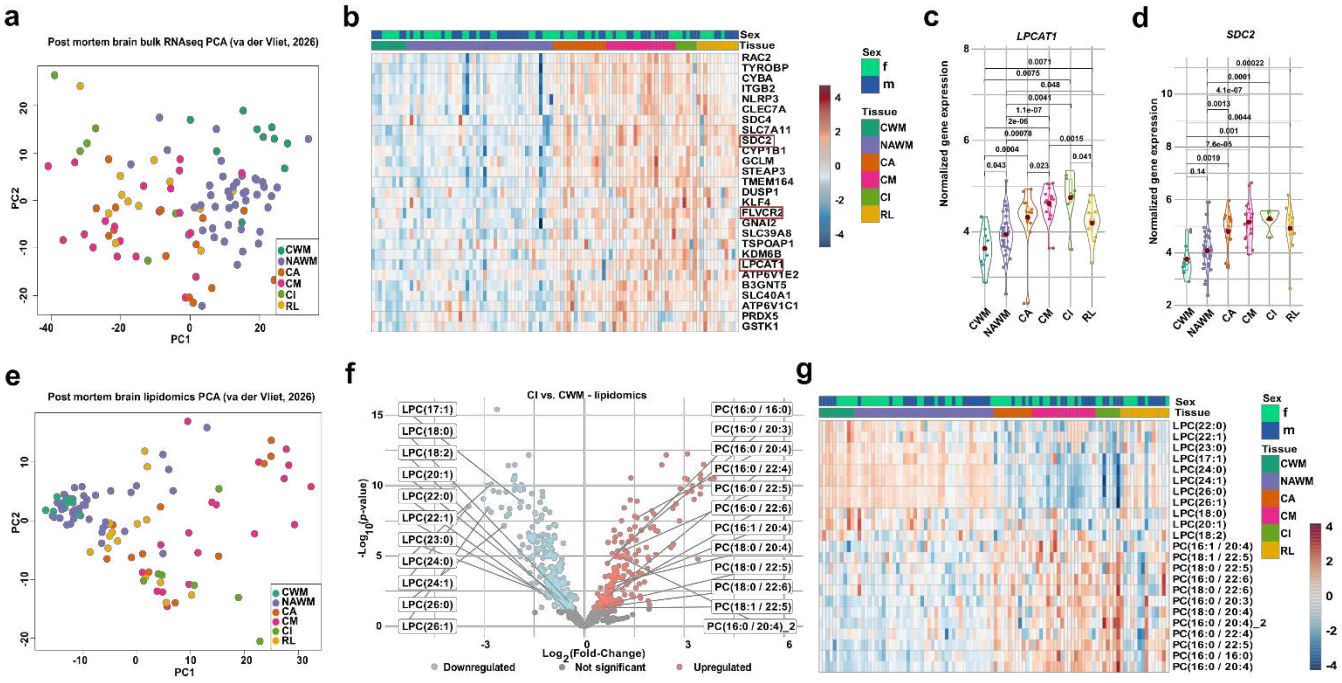
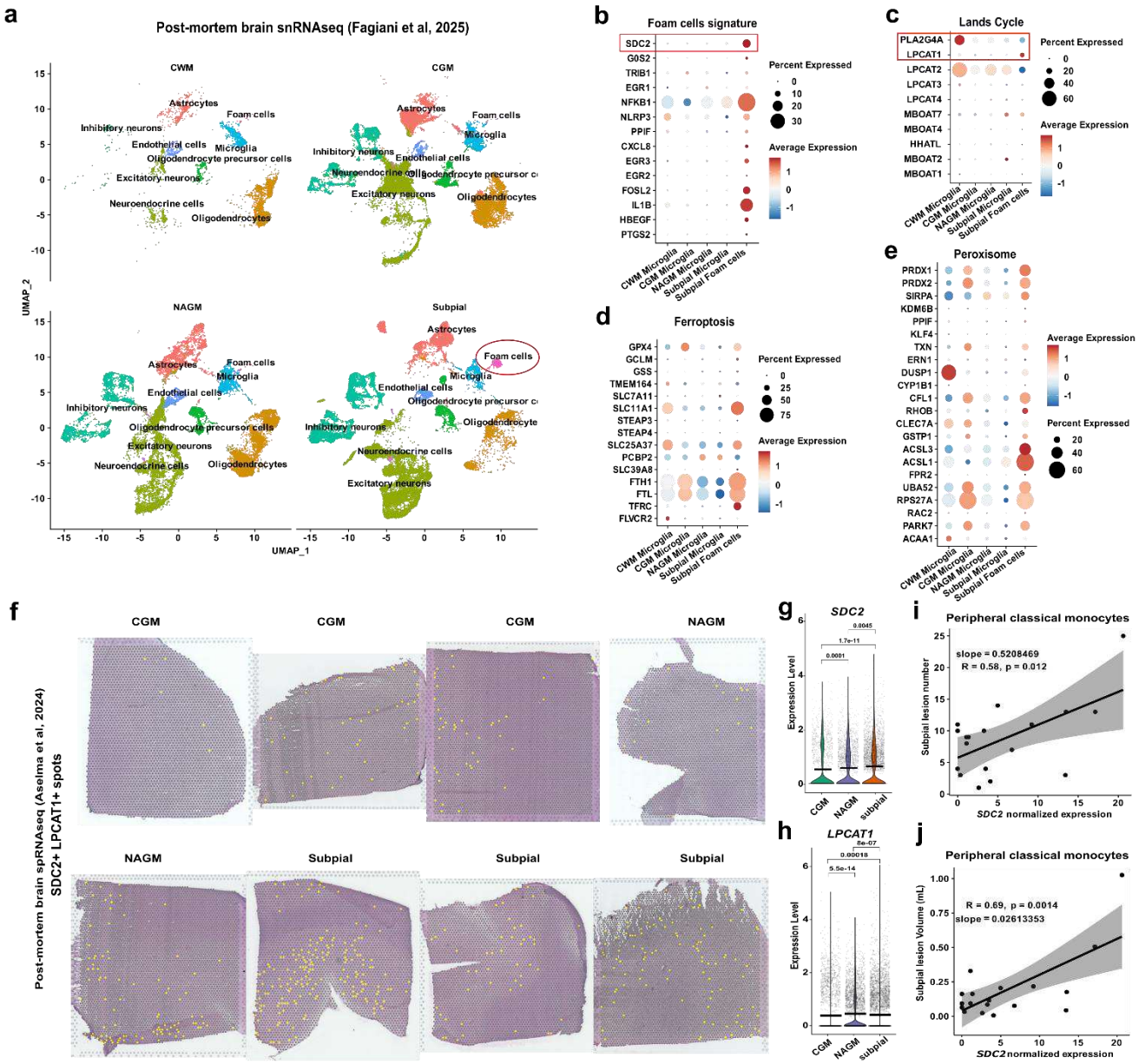
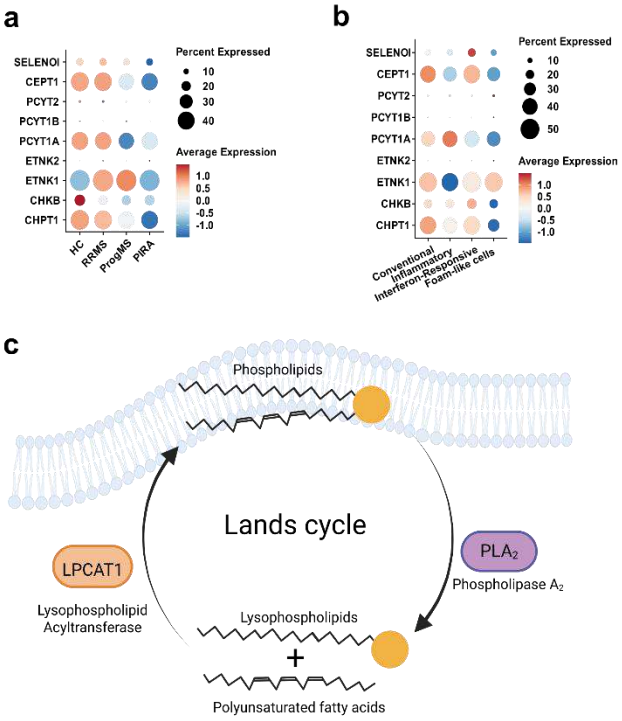

a
Post mortem brain bulk RNAseq PCA (va der Vliet, 2026)
PC1
PC2
CWM
NAWM
CA
CM
CI
RL
b
Sex
Tissue
RAC2
TYROBP
CYBA
ITGB2
NLRP3
CLEC7A
SDC4
SLC7A11
SDC2
CYP1B1
GCLM
STEAP3
TMEM164
DUSP1
KLF4
FLVCR2
GNAI2
SLC39A8
TSPOAP1
KDM6B
LPCAT1
ATP6V1E2
B3GNT5
SLC40A1
ATP6V1C1
PRDX5
GSTK1
c
LPCAT1
Normalized gene expression
d
SDC2
Normalized gene expression
e
Post mortem brain lipidomics PCA (va der Vliet, 2026)
f
CI vs. CWM - lipidomics
LPC(17:1)
LPC(18:0)
LPC(18:2)
LPC(20:1)
LPC(22:0)
LPC(22:1)
LPC(23:0)
LPC(24:0)
LPC(24:1)
LPC(26:0)
LPC(26:1)
PC(16:0 / 16:0)
PC(16:0 / 20:3)
PC(16:0 / 20:4)
PC(16:0 / 22:4)
PC(16:0 / 22:5)
PC(16:0 / 22:6)
PC(16:1 / 20:4)
PC(18:0 / 20:4)
PC(18:0 / 22:5)
PC(18:0 / 22:6)
PC(18:1 / 22:5)
PC(16:0 / 20:4)_2
Log2(Fold-Change)
-Log10(p-value)
Downregulated
Not significant
Upregulated
g
Sex
Tissue
LPC(22:0)
LPC(22:1)
LPC(23:0)
LPC(17:1)
LPC(24:0)
LPC(24:1)
LPC(26:0)
LPC(26:1)
LPC(18:0)
LPC(20:1)
LPC(18:2)
PC(16:1 / 20:4)
PC(18:1 / 22:5)
PC(18:0 / 22:5)
PC(16:0 / 22:6)
PC(18:0 / 22:6)
PC(16:0 / 20:3)
PC(18:0 / 20:4)
PC(16:0 / 20:4)_2
PC(16:0 / 22:4)
PC(16:0 / 22:5)
PC(16:0 / 16:0)
PC(16:0 / 20:4)

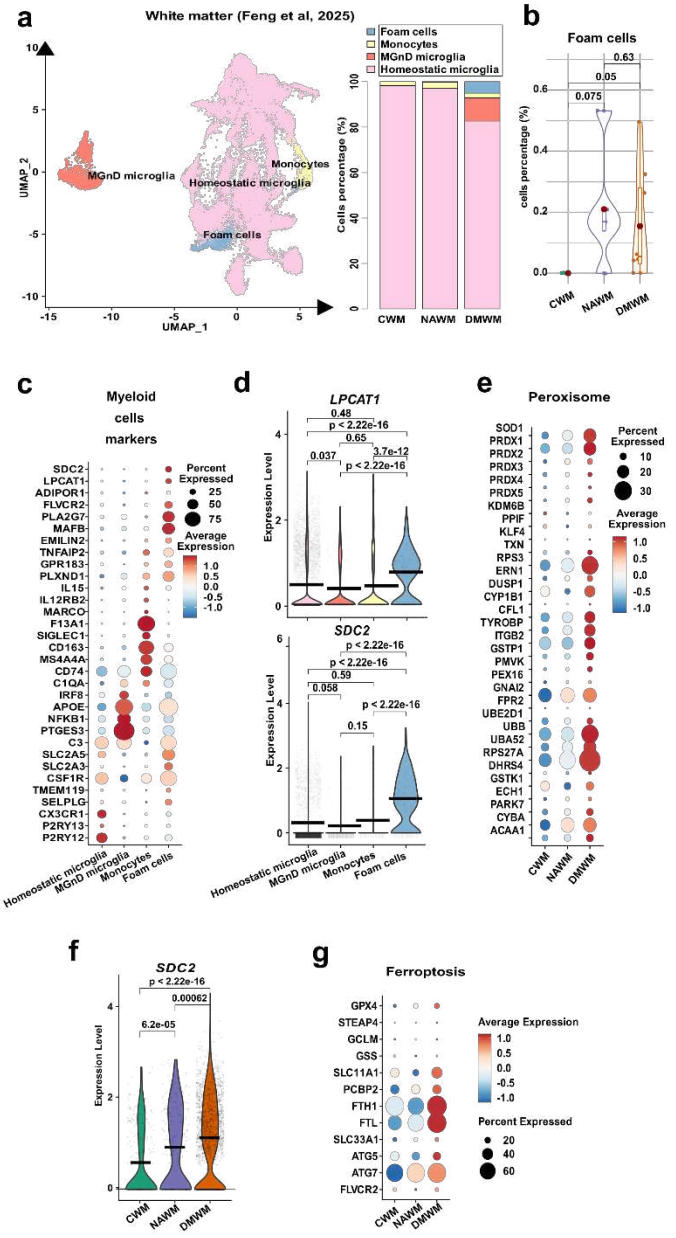
Fig. 6


a
Post-mortem brain snRNAseq (Fagiani et al, 2025)
CWM
CGM
NAGM
Subpial
Astrocytes
Foam cells
Inhibitory neurons
Endothelial cells
Microglia
Oligodendrocyte precursor cells
Excitatory neurons
Neuroendocrine cells
Oligodendrocytes
UMAP_1
UMAP_2
b
Foam cells signature
SDC2
G0S2
TRIB1
EGR1
NFKB1
NLRP3
PPIF
CXCL8
EGR3
EGR2
FOSL2
IL1B
HBEGF
PTGS2
Percent Expressed
Average Expression
CWM Microglia
CGM Microglia
NAGM Microglia
Subpial Microglia
Subpial Foam cells
c
Lands Cycle
PLA2G4A
LPCAT1
LPCAT2
LPCAT3
LPCAT4
MBOAT7
MBOAT4
HHATL
MBOAT2
MBOAT1
d
Ferroptosis
GPX4
GCLM
GSS
TMEM164
SLC7A11
SLC11A1
STEAP3
STEAP4
SLC25A37
PCBP2
SLC39A8
FTH1
FTL
TFRC
FLVCR2
e
Peroxisome
PRDX1
PRDX2
SIRPA
KDM6B
PPIF
KLF4
TXN
ERN1
DUSP1
CYP1B1
CFL1
RHOB
CLEC7A
GSTP1
ACSL3
ACSL1
FPR2
UBA52
RPS27A
RAC2
PARK7
ACAA1
f
CGM
NAGM
Subpial
Post-mortem brain spRNAseq (Aselma et al, 2024)
SDC2+ LPCAT1+ spots
g
SDC2
Expression Level
CGM
NAGM
subpial
h
LPCAT1
i
Peripheral classical monocytes
slope = 0.5208469
R = 0.58, p = 0.012
Subpial lesion number
SDC2 normalized expression
j
Peripheral classical monocytes
R = 0.69, p = 0.0014
slope = 0.02613353
Subpial lesion Volume (mL)
SDC2 normalized expression

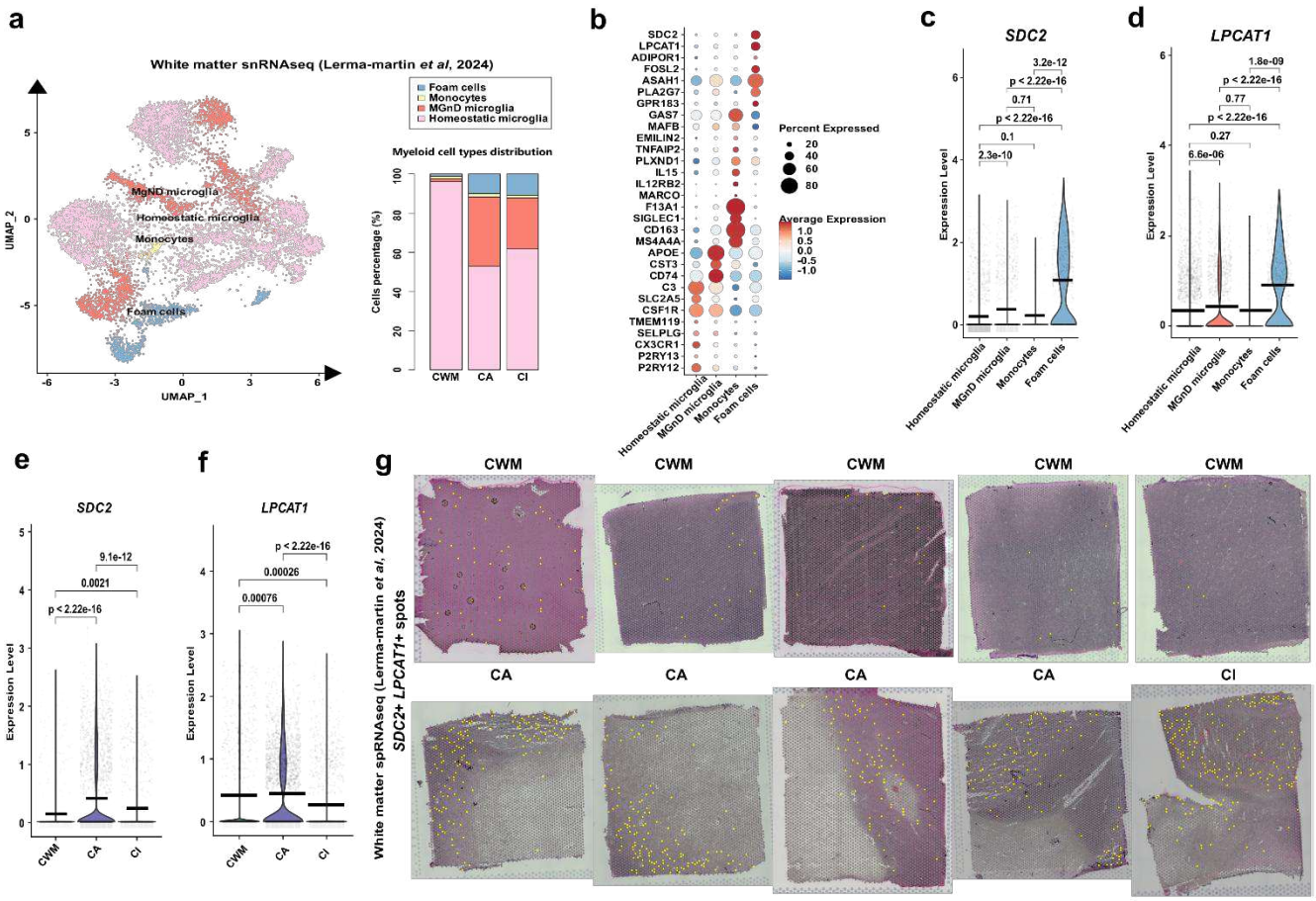
Extended Data Fig. 1



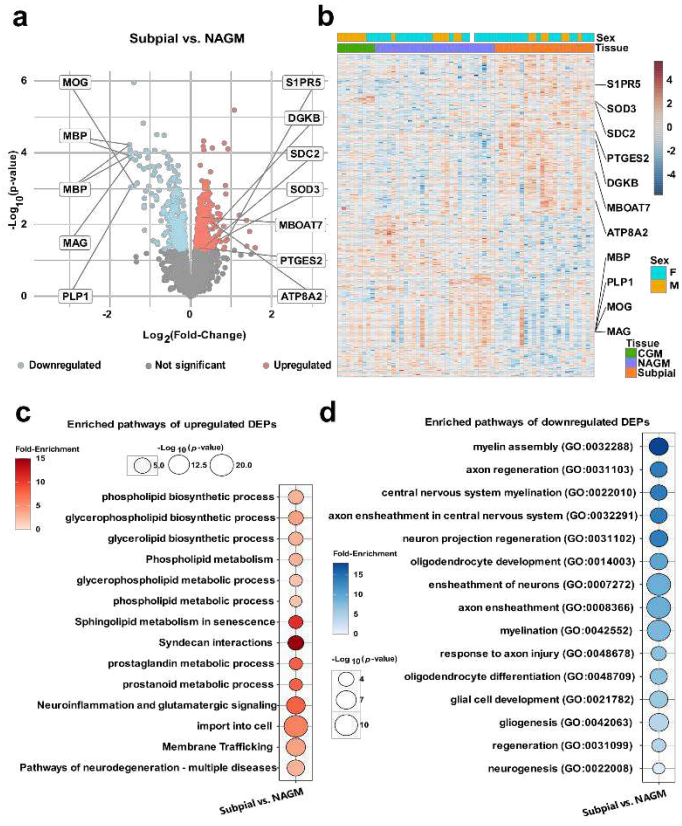
Extended Data Fig. 2



Extended Data Fig. 3



Extended Data Fig. 4



Extended Data Fig. 5

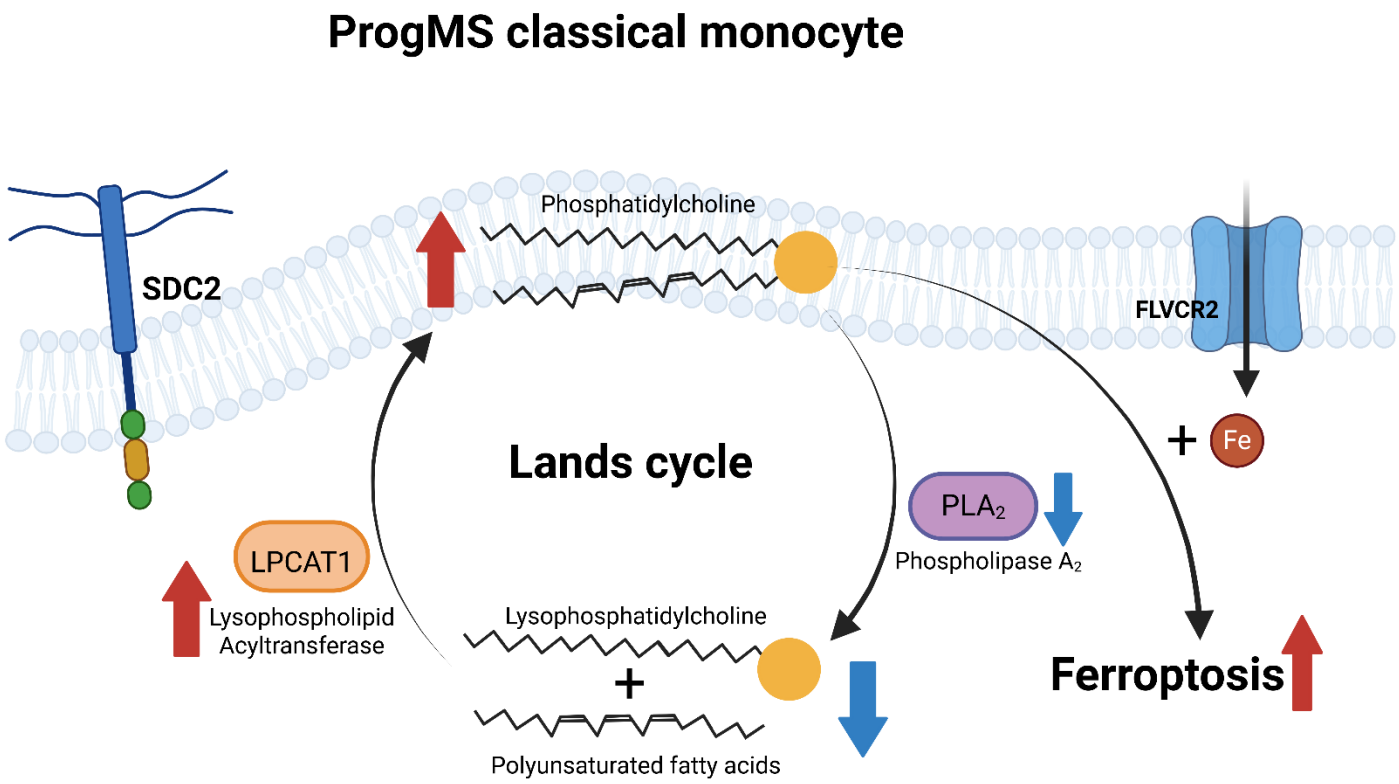


Figure captions

Fig. 1: SDC2+ foam-like classical monocytes are enriched in progressive MS and associate with disability worsening and PIRA.

a, Study design showing scRNA-seq analysis of myeloid-cell-enriched PBMCs from untreated healthy controls (HC; n = 6), patients with relapsing-remitting MS (RRMS; n = 10) and patients with progressive MS (ProgMS; n = 14). **b,** Longitudinal EDSS trajectories for study participants over 25 years. **c,** UMAP of peripheral myeloid cells annotated as classical, intermediate and nonclassical monocytes and monocyte-derived dendritic cells (mo-DCs). **d,e,** Relative abundance of classical monocytes (**d**) and nonclassical monocytes (**e**) determined by scRNA-seq and validated by flow cytometry in an independent cohort (HC, n = 6; RRMS, n = 9; ProgMS, n = 14). **f,** UMAP and marker-gene expression defining conventional, inflammatory, interferon-responsive and foam-like classical monocytes. **g,h,** Proportion of classical-monocyte subsets across diagnostic groups, with PIRA samples highlighted. **i,j,** Frequency of SDC2+ monocytes and SDC2 mean fluorescence intensity (MFI) on classical monocytes, with associations with EDSS. **k,l,** Expression of foam-like cell markers across diagnostic groups (**k**) and with PIRA samples separated as another group (**l**). **m,** Change in foam-like cell frequency in a longitudinally sampled ProgMS participant pre and post PIRA and its association with EDSS. **n,o,** Differential expression analysis of foam-like cell markers in classical monocytes obtained pre and post PIRA, highlighting SDC2. Each point represents one participant, unless otherwise indicated. In violin plots the center lines are median measurements, and center red dots are mean measurements. Statistical tests were Kruskal-Wallis test for multiple comparisons, considering it statistically different when $p<0.05$; exact p values are shown. Correlations were assessed using Spearman correlation; the correlation coefficient, two- sided p value, slope and fitted regression line with 95% confidence interval are shown.

Fig. 2: Altered Lands-cycle phospholipid remodeling promotes phosphatidylcholine accumulation in progressive MS classical monocytes.

a, Dot plot of pathways commonly enriched among genes upregulated in foam-like classical monocytes, ProgMS classical monocytes vs. RRMS and classical monocytes sampled post vs. pre PIRA, highlighting lipidic metabolism related pathways. **b,** Principal-component analysis of untargeted lipidomics profiles from classical monocytes of RRMS and ProgMS subjects. **c,d,** Volcano plot of differential abundance of lipid species (**c**) and

relative levels of lysophosphatidylcholines (LPCs) and phosphatidylcholines (PCs) shown in heatmap (**d**) in ProgMS vs. RRMS classical monocytes. **e,** Expression of Lands-cycle-associated genes in classical monocytes across the distinct subtypes Conventional, Inflammatory, Interferon-responsive and Foam-like cells (left), and across HC, RRMS, ProgMS and PIRA groups (right). **f,** *LPCAT1* and *PLA2G4A* expression in classical monocytes from one participant sampled pre and post PIRA. **g,** Differential abundance of serum PC precursors (LPC species, arachidonate and choline) in HC, stable RRMS (StRRMS), transition RRMS (TRRMS) and ProgMS groups in a previously published serum metabolomics cohort portrayed by heatmap. **h**, Volcano plot of serum metabolomics comparison between ProgMS and StRRMS subjects, highlighting PC precursors. Center lines in violin plots indicate median. Statistical tests were Wicoxon rank sum test for violins; exact *p* values are shown.

Fig. 3: Foam-like cells exhibit peroxisomal, inflammatory and ferroptosis-associated transcriptional programs.

a, Dot plot of pathways commonly enriched among genes upregulated in foam-like classical monocytes, ProgMS classical monocytes vs. RRMS and classical monocytes sampled post vs. pre PIRA, highlighting inflammatory, peroxisomal and ferroptosis-associated pathways. **b,** Expression of genes associated with peroxisomal activity across classical monocyte subsets (Conventional, Inflammatory, Interferon-responsive and Foam-like cells). **c,** Expression of peroxisomal activity-associated genes in classical monocytes from HC, RRMS, ProgMS and PIRA groups. **d,** Expression of iron-handling and ferroptosis-associated genes in classical monocytes across disease groups. **e,** Expression of ferroptosis-associated genes among classical-monocyte subsets (Conventional, Inflammatory, Interferon-responsive and Foam-like cells). Color scales indicate normalized gene expression. Statistical comparisons between cell types were performed using Wilcoxon rank sum test, whereas comparisons between diagnostic groups of subjects were performed using Kruskal-Wallis test.

Fig. 4: Foam cells in chronic white matter lesions share a Lands-cycle, ferroptosis and peroxisomal signature with peripheral foam-like monocytes.

a, UMAP of myeloid nuclei from control white matter (CWM), acute lesions (AL) and chronic active/inactive lesions (CA/CI), annotated as homeostatic microglia, microglia with neurodegenerative phenotype (MGnD), monocytes and foam cells (left), and stacked bar plot of myeloid cells percentage in each group (right). **b,**

Expression of markers used to define the indicated myeloid populations, including the foam cell marker *SDC2*. **c-e,** Expression of Lands-cycle-associated genes (**c**), ferroptosis-associated genes (**d**) and peroxisomal activity-associated genes (**e**) by lesion group and myeloid-cell population. **f,** Spatial transcriptomic localization of *SDC2* and *LPCAT1* coexpressing spots in CWM, normal-appearing white matter (NAWM), CA and CI tissue, overlaid on Luxol fast blue staining; differential expression of *SDC2* and *LPCAT1* is shown. **g,** Volcano plot of differential abundance of untargeted metabolites, comparing ProgMS lesion core vs. CWM, highlighting arachidonate, choline-containing metabolites, lysophospholipids and lecithins. **h,** Relative levels of arachidonate, choline-containing metabolites, lysophospholipids and lecithins across CWM, NAWM and chronic-lesion regions. Images are representative of 14 tissue sections from 14 donors. Color scales indicate normalized gene or metabolite expressions in z scale. Comparisons between tissue types were performed using Kruskal-Wallis test; exact *p* values are shown.

Fig. 5: Remyelinating lesions exhibit partial restoration of the chronic-lesion lipidomic phenotype.

a, Principal-component analysis of bulk RNA-seq profiles from CWM, NAWM, chronic active (CA), mixed chronic active/inactive (CM), chronic inactive (CI) and remyelinating lesions (RL). **b,** Heatmap of upregulated genes in tissue with lesion compared with tissue without lesion, highlighting *SDC2*, *LPCAT1* and *FLVCR2*. **c,d,** Violin plot showing the expression of *LPCAT1* (**c**) and *SDC2* (**d**) across tissue types. **e,** Principal-component analysis of lipidomic profiles from the indicated tissue groups. **f,** Volcano plot of differential abundance of untargeted lipids comparing CI vs. CWM, highlighting LPC and PC species. **g,** Relative abundance of LPC and PC species across tissues with and without lesion, showing convergence of RL with CWM and NAWM. Each point represents one tissue sample from donors in PCA and violin plots. Comparisons between tissue types were performed using Kruskal-Wallis test; exact *p* values are shown.

Fig. 6: *SDC2*+ foam cells are enriched in subpial lesions and associate with subpial lesion burden.

a, UMAP of brain nuclei from CWM, control gray matter (CGM), MS normal-appearing gray matter (NAGM) and subpial lesions, displayed by tissue group, and grouped by assigned cell type. **b-e,** Expression of Foam cells marker-genes (**b**), Lands-cycle-associated genes (**c**), ferroptosis-associated genes (**d**) and peroxisomal activity-associated genes (**e**) in subpial foam cells relative to populations of microglia from each brain tissue. **f,** Spatial distribution of *SDC2* and *LPCAT1* coexpressing spots in CGM, NAGM and subpial lesions, overlaid on

histological images. **g,h,** Spatial transcriptomic expression of *SDC2* (**g**) and *LPCAT1* (**h**) across gray matter tissue groups. **i,j,** Associations between *SDC2* expression in peripheral classical monocytes and subpial lesion number (**i**) or volume (**j**) measured by 7 T MRI in CLIMB participants (n = 18). Images are representative of 8 sections from 8 donors. Correlations were assessed using Pearson correlation; the correlation coefficient, two-sided *p* value, slope and fitted regression line with 95% confidence interval are shown.

Extended Data Fig. 1: CDP-Choline pathway gene expression and Lands cycle schematic model

a,b, Expression of CDP-Choline pathway-associated genes in classical monocytes across HC, RRMS, ProgMS and PIRA groups (**a**), and across the distinct subtypes Conventional, Inflammatory, Interferon-responsive and Foam-like cells (**b**). **c,** In the Lands cycle, lysophospholipid acyltransferases, as LPCAT1, reacylate lysophospholipids with long-chain fatty acids to regenerate phospholipids that will be incorporated in cellular membrane, whereas phospholipases (PLA_2) hydrolyze phospholipids to release long-chain fatty acids and generate lysophospholipid intermediates into the cytoplasm.

Extended Data Fig. 2: Independent snRNA-seq analysis identifies foam cells with Lands-cycle, ferroptosis and peroxisomal signatures in demyelinated MS white matter.

a, UMAP of myeloid nuclei from control white matter (CWM), normal-appearing white matter (NAWM) and MS demyelinated white matter (DMWM), annotated as homeostatic microglia, microglia with neurodegenerative phenotype (MGnD), monocytes and foam cells (left), and stacked bar plot of myeloid cells percentage in each group (right). **b,** Relative abundance of the foam cell population in each sample across tissue groups. **c,** Expression of markers used to define the indicated myeloid populations, including the foam cell marker *SDC2*. **d,** Violin plots showing the differential expression of *LPCAT1* (top) and *SDC2* (bottom) comparing the distinct identified cell types. **e,** Expression of peroxisomal activity-associated genes in myeloid cells from CWM, NAWM and DMWM. **f,** Violin plot showing the differential expression of *SDC2* comparing the CWM, NAWM and DMWM tissue types. **g,** Expression of ferroptosis-associated genes in myeloid cells from CWM, NAWM and DMWM. Results derive from an independent publicly available postmortem human white matter single-nucleus RNA-seq dataset. Color scales indicate normalized gene expression in z-scale. Statistical testing was performed using Kruskal-Wallis test, with adjustment for multiple comparisons as indicated; exact *p* values are shown.

Extended Data Fig. 3: Independent snRNAseq and spRNAseq validation of SDC2+ LPCAT1+ foam-cell-associated spots in chronic MS white matter lesions.

a, UMAP of myeloid nuclei snRNAseq from control white matter (CWM), chronic active lesion (CA) and chronic inactive lesion (CI), annotated as homeostatic microglia, microglia with neurodegenerative phenotype (MGnD), monocytes and foam cells (left), and stacked bar plot of myeloid cells percentage in each group (right) from an independent postmortem MS white matter dataset. **b,** Expression of markers used to define the indicated myeloid populations, including the foam cell marker *SDC2*. **c,d,** Violin plots showing the differential expression of *SDC2* (**c**) and *LPCAT1* (**d**) comparing the distinct identified cell types. **e,f,** Violin plots showing the differential expression of *SDC2* (**e**) and *LPCAT1* (**f**) in the myeloid cells from CWM, CA and CI. **g,** Spatial transcriptomic maps showing *SDC2* and *LPCAT1* coexpressing spots in CWM, CA and CI lesions from the same independent postmortem MS white matter dataset. Images are representative of 10 sections from 10 donors. Center lines in the violin plots indicate the median. Color scales indicate normalized gene expression in z-scale. Statistical testing was performed using Kruskal-Wallis test, with adjustment for multiple comparisons as indicated; exact *p* values are shown.

Extended Data Fig. 4: Proteomic evidence of elevated SDC2 and phospholipid metabolism pathways in subpial MS lesions.

a, Volcano plot of differential abundance of untargeted proteins, comparing subpial lesions vs. normal-appearing gray matter (NAGM), highlighting proteins involved in myelin composition, Lands cycle, inflammation and peroxisome activity, and SDC2. **b,** Relative levels of differential enriched proteins in subpial lesions vs. tissue without lesion (CGM and NAGM) across samples from each tissue type, highlighting proteins involved in myelin composition, Lands cycle, inflammation and peroxisome activity, and SDC2. **c,** Pathway enrichment analysis of proteins increased in subpial lesions relative to NAGM, identifying pathways associated with phospholipid metabolism and syndecan interactions. **d,** Pathway enrichment analysis of proteins decreased in subpial lesions relative to NAGM, identifying pathways associated with myelination, neurogenesis and regeneration of lesioned tissue. Data were obtained from a publicly available postmortem human MS proteomic dataset. Differential protein abundance was performed using ANCOVA with gender and age as covariates. Pathway enrichment analyses was performed through ORA.

Extended Data Fig. 5: Proposed model of a systemic SDC2+ foam-cell program in progressive MS and PIRA.

In peripheral blood, a subset of classical monocytes acquires an SDC2+ foam-like cell phenotype characterized by increased expression of lipid-handling genes, including *LPCAT1*, and reduced expression of *PLA2G4A*. This pattern is associated with reduced lysophosphatidylcholine (LPC) availability and increased phosphatidylcholine (PC) accumulation, consistent with altered Lands-cycle phospholipid remodeling. Increased expression of genes involved in iron transport, redox regulation, peroxisomal activity and ferroptosis-associated pathways may further promote a lipid-peroxidation-prone state. A transcriptionally and metabolically related foam-cell population is enriched in chronic active/inactive white matter lesions and subpial lesions, where SDC2+ LPCAT1+ spatial transcriptomic spots localize to or around demyelinated tissue. The model summarizes associations supported by the present analyses and does not imply direct trafficking or lineage conversion of circulating SDC2+ monocytes into lesion-resident foam cells.

REFERENCES

1. L. Kappos *et al.*, Contribution of Relapse-Independent Progression vs Relapse-Associated Worsening to Overall Confirmed Disability Accumulation in Typical Relapsing Multiple Sclerosis in a Pooled Analysis of 2 Randomized Clinical Trials. *JAMA Neurol* **77**, 1132-1140 (2020).
2. B. A. C. Cree *et al.*, Silent progression in disease activity-free relapsing multiple sclerosis. *Ann Neurol* **85**, 653-666 (2019).
3. M. Absinta *et al.*, Association of Chronic Active Multiple Sclerosis Lesions With Disability In Vivo. *JAMA Neurol* **76**, 1474-1483 (2019).
4. H. Lassmann, Multiple Sclerosis Pathology. *Cold Spring Harb Perspect Med* **8**, (2018).
5. I. D. Kilsdonk *et al.*, Morphological features of MS lesions on FLAIR* at 7 T and their relation to patient characteristics. *J Neurol* **261**, 1356-1364 (2014).
6. B. Rossi, B. Santos-Lima, E. Terrabuio, E. Zenaro, G. Constantin, Common Peripheral Immunity Mechanisms in Multiple Sclerosis and Alzheimer's Disease. *Front Immunol* **12**, 639369 (2021).
7. V. Radushev *et al.*, Dysregulated cytokine and oxidative response in hyper-glycolytic monocytes in obesity. *Front Immunol* **15**, 1416543 (2024).
8. N. Raulien *et al.*, Fatty Acid Oxidation Compensates for Lipopolysaccharide-Induced Warburg Effect in Glucose-Deprived Monocytes. *Front Immunol* **8**, 609 (2017).
9. D. van der Vliet *et al.*, Foamy microglia link oxylipins to disease progression in multiple sclerosis. *Nat Neurosci* **29**, 1585-1598 (2026).
10. R. Corrêa *et al.*, Lysophosphatidylcholine Induces NLRP3 Inflammasome-Mediated Foam Cell Formation and Pyroptosis in Human Monocytes and Endothelial Cells. *Front Immunol* **10**, 2927 (2019).
11. C. Moessinger, L. Kuerschner, J. Spandl, A. Shevchenko, C. Thiele, Human lysophosphatidylcholine acyltransferases 1 and 2 are located in lipid droplets where they catalyze the formation of phosphatidylcholine. *J Biol Chem* **286**, 21330-21339 (2011).

12. Y. Kita, H. Shindou, T. Shimizu, Cytosolic phospholipase A. *Biochim Biophys Acta Mol Cell Biol Lipids* **1864**, 838-845 (2019).
13. W. Li *et al.*, Foam cell death induced by 7beta-hydroxycholesterol is mediated by labile iron-driven oxidative injury: mechanisms underlying induction of ferritin in human atheroma. *Free Radic Biol Med* **39**, 864-875 (2005).
14. J. Cai *et al.*, Iron accumulation in macrophages promotes the formation of foam cells and development of atherosclerosis. *Cell Biosci* **10**, 137 (2020).
15. S. J. Dixon *et al.*, Ferroptosis: an iron-dependent form of nonapoptotic cell death. *Cell* **149**, 1060-1072 (2012).
16. D. Tang, G. Kroemer, Peroxisome: the new player in ferroptosis. *Signal Transduct Target Ther* **5**, 273 (2020).
17. B. B. Boyanovsky, P. Shridas, M. Simons, D. R. van der Westhuyzen, N. R. Webb, Syndecan-4 mediates macrophage uptake of group V secretory phospholipase A2-modified LDL. *J Lipid Res* **50**, 641-650 (2009).
18. L. C. Wilsie, A. M. Gonzales, R. A. Orlando, Syndecan-1 mediates internalization of apoE-VLDL through a low density lipoprotein receptor-related protein (LRP)-independent, non-clathrin-mediated pathway. *Lipids Health Dis* **5**, 23 (2006).
19. E. I. Leonova, O. V. Galzitskaya, Role of Syndecans in Lipid Metabolism and Human Diseases. *Adv Exp Med Biol* **855**, 241-258 (2015).
20. J. E. Vance, D. E. Vance, Phospholipid biosynthesis in mammalian cells. *Biochem Cell Biol* **82**, 113-128 (2004).
21. D. Hishikawa, T. Hashidate, T. Shimizu, H. Shindou, Diversity and function of membrane glycerophospholipids generated by the remodeling pathway in mammalian cells. *J Lipid Res* **55**, 799-807 (2014).
22. C. R. McMaster, From yeast to humans - roles of the Kennedy pathway for phosphatidylcholine synthesis. *FEBS Lett* **592**, 1256-1272 (2018).
23. C. Moessinger *et al.*, Two different pathways of phosphatidylcholine synthesis, the Kennedy Pathway and the Lands Cycle, differentially regulate cellular triacylglycerol storage. *BMC Cell Biol* **15**, 43 (2014).
24. L. A. Schwerdtfeger *et al.*, Gut microbiota and metabolites are linked to disease progression in multiple sclerosis. *Cell Rep Med* **6**, 102055 (2025).
25. L. Schirmer *et al.*, Neuronal vulnerability and multilineage diversity in multiple sclerosis. *Nature* **573**, 75-82 (2019).
26. S. Klistorner *et al.*, Expansion of chronic lesions is linked to disease progression in relapsing-remitting multiple sclerosis patients. *Mult Scler* **27**, 1533-1542 (2021).
27. A. Dal-Bianco, J. Oh, P. Sati, M. Absinta, Chronic active lesions in multiple sclerosis: classification, terminology, and clinical significance. *Ther Adv Neurol Disord* **17**, 17562864241306684 (2024).
28. R. Feng *et al.*, Single-cell spatial transcriptomic profiling defines a pathogenic inflammatory niche in chronic active multiple sclerosis lesions. *Immunity* **58**, 2989-3005.e2910 (2025).
29. A. M. Alsema *et al.*, Spatially resolved gene signatures of white matter lesion progression in multiple sclerosis. *Nat Neurosci* **27**, 2341-2353 (2024).
30. C. Lerma-Martin *et al.*, Cell type mapping reveals tissue niches and interactions in subcortical multiple sclerosis lesions. *Nat Neurosci* **27**, 2354-2365 (2024).
31. D. C. Ladakis *et al.*, Metabolomics of Multiple Sclerosis Lesions Demonstrates Lipid Changes Linked to Alterations in Transcriptomics-Based Cellular Profiles. *Neurol Neuroimmunol Neuroinflamm* **11**, e200219 (2024).
32. E. S. Beck *et al.*, Contribution of new and chronic cortical lesions to disability accrual in multiple sclerosis. *Brain Commun* **6**, fcae158 (2024).
33. C. A. Treaba *et al.*, Longitudinal Characterization of Cortical Lesion Development and Evolution in Multiple Sclerosis with 7.0-T MRI. *Radiology* **291**, 740-749 (2019).
34. E. S. Beck *et al.*, Cortical lesion hotspots and association of subpial lesions with disability in multiple sclerosis. *Mult Scler* **28**, 1351-1363 (2022).
35. F. Fagiani *et al.*, Spatially-restricted inflammation-induced senescent-like glia in multiple sclerosis and patient-derived organoids. *Nat Commun* **16**, 8477 (2025).
36. M. Kaufmann *et al.*, Identification of early neurodegenerative pathways in progressive multiple sclerosis. *Nat Neurosci* **25**, 944-955 (2022).
37. G. M. Tannahill, N. Iraci, E. Gaude, C. Frezza, S. Pluchino, Metabolic reprograming of mononuclear phagocytes in progressive multiple sclerosis. *Front Immunol* **6**, 106 (2015).
38. L. Peruzzotti-Jametti, C. M. Willis, R. Hamel, G. Krzak, S. Pluchino, Metabolic Control of Smoldering Neuroinflammation. *Front Immunol* **12**, 705920 (2021).
39. K. M. Gillen, M. Mubarak, T. D. Nguyen, D. Pitt, Significance and In Vivo Detection of Iron-Laden Microglia in White Matter Multiple Sclerosis Lesions. *Front Immunol* **9**, 255 (2018).

40. F. Bagnato *et al.*, Imaging chronic active lesions in multiple sclerosis: a consensus statement. *Brain* **147**, 2913-2933 (2024).
41. E. Van San *et al.*, Ferroptosis contributes to multiple sclerosis and its pharmacological targeting suppresses experimental disease progression. *Cell Death Differ* **30**, 2092-2103 (2023).
42. F. D. Lublin *et al.*, The 2013 clinical course descriptors for multiple sclerosis: A clarification. *Neurology* **94**, 1088-1092 (2020).
43. S. A. Gauthier, B. I. Glanz, M. Mandel, H. L. Weiner, A model for the comprehensive investigation of a chronic autoimmune disease: the multiple sclerosis CLIMB study. *Autoimmun Rev* **5**, 532-536 (2006).
44. J. Müller *et al.*, Standardized Definition of Progression Independent of Relapse Activity (PIRA) in Relapsing-Remitting Multiple Sclerosis. *JAMA Neurol* **82**, 614-625 (2025).
45. J. Müller *et al.*, Harmonizing Definitions for Progression Independent of Relapse Activity in Multiple Sclerosis: A Systematic Review. *JAMA Neurol* **80**, 1232-1245 (2023).
46. L. Kappos *et al.*, Greater sensitivity to multiple sclerosis disability worsening and progression events using a roving versus a fixed reference value in a prospective cohort study. *Mult Scler* **24**, 963-973 (2018).
47. J. Kim *et al.*, A Subpopulation of Monocytes in Normal Human Blood Has Significant Magnetic Susceptibility: Quantification and Potential Implications. *Cytometry A* **95**, 478-487 (2019).
48. Y. Hao *et al.*, Integrated analysis of multimodal single-cell data. *Cell* **184**, (2021).
49. G. Finak *et al.*, MAST: a flexible statistical framework for assessing transcriptional changes and characterizing heterogeneity in single-cell RNA sequencing data. *Genome biology* **16**, (2015).
50. M. V. Kuleshov *et al.*, Enrichr: a comprehensive gene set enrichment analysis web server 2016 update. *Nucleic Acids Res* **44**, W90-97 (2016).
51. Z. Xie *et al.*, Gene Set Knowledge Discovery with Enrichr. *Curr Protoc* **1**, e90 (2021).
52. C. M. T. Edward Y Chen, Yan Kou, Qiaonan Duan, Zichen Wang, Gabriela Vaz Meirelles, Neil R Clark and Avi Ma'ayan, Enrichr: interactive and collaborative HTML5 gene list enrichment analysis tool. *BMC Bioinformatics* **128**, (2013).
53. H. Mi *et al.*, Protocol Update for Large-Scale Genome and Gene Function Analysis With the PANTHER Classification System (v.14.0). *Nature protocols* **14**, (2019).
54. J. M. Elizarraras *et al.*, WebGestalt 2024: faster gene set analysis and new support for metabolomics and multi-omics. *Nucleic Acids Res* **52**, W415-W421 (2024).
55. M. I. Love, W. Huber, S. Anders, Moderated estimation of fold change and dispersion for RNA-seq data with DESeq2. *Genome Biology* **15**, 550 (2014).

Supplementary Files

This is a list of supplementary files associated with this preprint. Click to download.

- SuppTable1.xlsx